

# A Potential Enstrophy and Energy Conserving Scheme for the Shallow-Water Equations Extended to Generalized Curvilinear Coordinates

MICHAEL D. TOY AND RAMACHANDRAN D. NAIR

*Institute for Mathematics Applied to Geosciences, National Center for Atmospheric Research,<sup>a</sup> Boulder, Colorado*

(Manuscript received 29 June 2016, in final form 3 October 2016)

## ABSTRACT

An energy and potential enstrophy conserving finite-difference scheme for the shallow-water equations is derived in generalized curvilinear coordinates. This is an extension of a scheme formulated by Arakawa and Lamb for orthogonal coordinate systems. The starting point for the present scheme is the shallow-water equations cast in generalized curvilinear coordinates, and tensor analysis is used to derive the invariant conservation properties. Preliminary tests on a flat plane with doubly periodic boundary conditions are presented. The scheme is shown to possess similar order-of-convergence error characteristics using a non-orthogonal coordinate compared to Cartesian coordinates for a nonlinear test of flow over an isolated mountain. A linear normal mode analysis shows that the discrete form of the Coriolis term provides stationary geostrophically balanced modes for the nonorthogonal coordinate and no unphysical computational modes are introduced. The scheme uses centered differences and averages, which are formally second-order accurate. An empirical test with a steady geostrophically balanced flow shows that the convergence rate of the truncation errors of the discrete operators is second order. The next step will be to adapt the scheme for use on the cubed sphere, which will involve modification at the lateral boundaries of the cube faces.

## 1. Introduction

Arakawa and Lamb (1981, hereafter AL81) developed a finite-difference scheme for the shallow-water equations that simultaneously conserves energy and potential enstrophy. As pointed out in subsequent work (e.g., Salmon 2004), this was a significant achievement because neither kinetic energy nor potential enstrophy are simple quadratic quantities due to the divergent nature of shallow-water motion. Conserving analogs of these two global invariants in numerical models is known to prevent a spurious cascade of energy toward small scales. Direct application of AL81's scheme, which was derived in rectangular Cartesian coordinates, is limited to orthogonal, quadrilateral grids; however, it has inspired an active field of research in the development of schemes that conserve higher-order invariants on generalized grids.

AL81's scheme can be applied directly to global models that use latitude–longitude grids; however, such

grids suffer from excessive clustering of grid points near the poles, which can severely limit the size of the time step that can be taken. Alternative grid structures with a quasi-uniform distribution of points have been developed to overcome this problem; these include the cubed sphere (Sadourny 1972; Ronchi et al. 1996), the icosahedral geodesic grid (Sadourny et al. 1968; Williamson 1968; Heikes and Randall 1995a,b; Satoh et al. 2008; Lee and MacDonald 2009; Bleck et al. 2015), triangular grids (Bonaventura and Ringler 2005; Gassmann 2011), and arbitrarily structured grids based on Voronoi tessellations (Stuhne and Peltier 2006; Thuburn et al. 2009).

The numerical techniques of AL81, developed for finite-difference equations on orthogonal, quadrilateral grids, do not easily carry over to these alternative grid structures, so new techniques have been developed to conserve the various invariant quantities. For example, Ringler and Randall (2002) designed discrete analogs of the divergence and curl operators based on their fundamental, coordinate-invariant definitions that achieve energy and potential-enstrophy conservation for the shallow-water equations on a geodesic grid. In Thuburn et al. (2009) and Ringler et al. (2010), a conservative scheme, known as TRiSK, was formulated for arbitrarily

<sup>a</sup> The National Center for Atmospheric Research is sponsored by the National Science Foundation.

Corresponding author e-mail: Michael D. Toy, toy@ucar.edu

structured locally orthogonal grids. In a follow-up paper, [Thuburn and Cotter \(2012\)](#) extended TRiSK to non-orthogonal grids and formalized the method as a type of discrete exterior calculus (DEC) method ([Hirani 2003](#)); however the discretization does not conserve potential enstrophy. [Weller \(2014\)](#) also developed a scheme for nonorthogonal, arbitrary polygonal grids that nearly conserves energy and potential enstrophy. In that paper, a quasi-orthogonal diamond grid for the cubed sphere was also developed that minimizes errors inherent with grid nonorthogonality. An issue that arises with these schemes is a lack of consistency (i.e., zeroth-order accuracy) of some of the discrete operators. This issue has been analyzed on various grids, including cubed-sphere grids, in [Weller \(2014\)](#) and [Thuburn et al. \(2014\)](#).

In a different approach, [Salmon \(2004, 2007\)](#) developed energy and potential enstrophy conserving schemes for the shallow-water equations on regular square grids and unstructured triangular grids using Hamiltonian fluid dynamics. For square grids, Salmon showed that AL81's scheme can be derived using this generalized method. [Eldred \(2015\)](#) extended AL81's scheme to arbitrary nonorthogonal polygonal grids by combining Hamiltonian and DEC methods, embodying the energy and potential-enstrophy conserving properties of AL81.

In this paper, we revisit the approach of AL81 for quadrilateral grids, but instead of starting with the vector-invariant system of equations in rectangular Cartesian coordinates, we start with the system expressed in generalized curvilinear coordinates. The result is a finite-difference scheme that exactly conserves mass, energy, and potential enstrophy on generalized (including nonorthogonal) quadrilateral grids with a form almost identical to AL81. In fact, the weightings of potential vorticity in the momentum equations, which are responsible for potential enstrophy conservation, are identical in both schemes. Going to generalized nonorthogonal coordinates is complicated by the expression for kinetic energy involving products of two sets of velocity components: the covariant and contravariant components, the former being prognostic variables and the latter being diagnostic (e.g., [Tort et al. 2015](#)). Proper diagnosis of the contravariant components leads to kinetic energy conservation. Despite this complication, the scheme still possesses the conceptual simplicity of the AL81 discretization. Also, it is still based on centered differences and averages, which are formally second-order accurate. At this point, the scheme has been formulated and tested on a plane surface with doubly periodic boundary conditions; however, we propose that it could be modified for application on the cubed

sphere, the challenge being to correctly handle the edges and corners connecting the cube faces. The scheme could then make use of cubic grids based on curvilinear coordinate systems for each of the faces, such as those based on gnomonic (central) projections ([Sadourny 1972](#); [Ronchi et al. 1996](#)), which include the equiangular projections used by [Nair et al. \(2005a,b\)](#), or conformal (angle preserving) mappings ([Rančić et al. 1996](#); [McGregor 1996](#); [Adcroft et al. 2004](#)).

In section 2 of the paper, we describe the continuous shallow-water equations in generalized curvilinear coordinates and, using tensor analysis, we derive the tendency equations for energy, potential vorticity, and potential enstrophy. In section 3, we derive a finite-difference scheme that conserves both energy and potential enstrophy on the staggered Arakawa C grid. Our starting point for potential enstrophy conservation is AL81's scheme itself, and we demonstrate that a particular form of diagnosing the contravariant velocity components leads to kinetic energy conservation. In section 4, as a first step toward applying the new scheme to the sphere, we test the discrete equations in a shallow-water model on a plane surface with doubly periodic lateral boundary conditions using a simple, nonorthogonal coordinate transformation. First, we analyze the linear characteristics of the scheme to show that there are no unphysical computational modes introduced by the transformation to generalized coordinates, that the normal modes are all stable, and that stationary geostrophic modes remain stationary in the discrete system. We then present results of a nonlinear test of flow over an isolated mountain in order to demonstrate the conservation properties of the numerical scheme. The results with the nonorthogonal coordinate compare well with those of a run with Cartesian coordinates (i.e., the original scheme in AL81). We also compare the resolution-dependent error convergence between the two coordinate systems and show that the order of convergence is basically maintained by the extended scheme in AL81, although the error is larger with the nonorthogonal coordinate system. The model is then tested under steady-state nonlinear geostrophic flow in which the exact solution is known, and the overall discretization error as well as the local truncation errors of each of the terms in the model equations are shown to possess second-order convergence. Finally, we provide a summary and discussion in section 5.

## 2. Continuous equations

To introduce the basic notations for our derivations, we first consider a general 2D coordinate transformation using classical tensor analysis (e.g., [Dutton 1986](#); [Warsi 2006](#); [Wesseling 2009](#)).

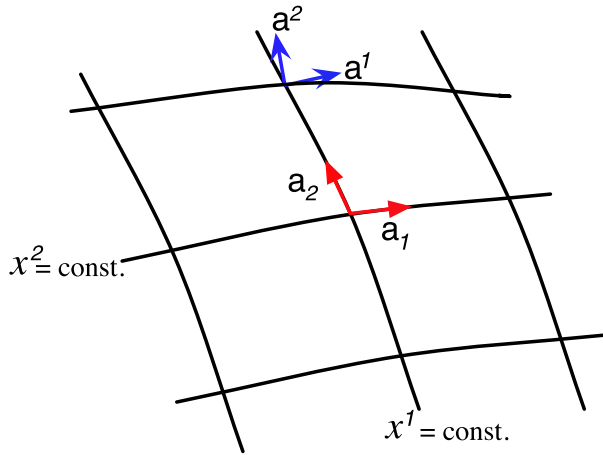


FIG. 1. Schematic diagram illustrating a nonorthogonal curvilinear  $(x^1, x^2)$  grid system and the basis vectors in physical space. The covariant basis vector  $\mathbf{a}_i$  (where  $i = 1, 2$ ) is a tangential vector (red), which points along a coordinate line, while the contravariant basis vector  $\mathbf{a}^i$  (blue) points normally to a coordinate line.

*a. Nonorthogonal curvilinear geometry*

Consider the coordinate transformation  $(x, y) \rightarrow (x^1, x^2)$ , where  $x$  and  $y$  are the rectangular Cartesian coordinates and  $x^1 = f_1(x, y)$  and  $x^2 = f_2(x, y)$ . In general, the coordinate transformation gives rise to two sets of basis vectors: the ‘‘covariant’’ basis vectors,

$$\mathbf{a}_i = \frac{\partial \mathbf{x}}{\partial x^i}, \tag{1}$$

and the ‘‘contravariant’’ basis vectors,

$$\mathbf{a}^i = \nabla x^i, \tag{2}$$

where  $\mathbf{x}$  is the position vector,  $\nabla$  is the horizontal gradient operator, and  $i = 1, 2$  is the dimensional index. The covariant metric tensor associated with the transformation is defined as  $\mathbf{G}_{ij} = \mathbf{a}_i \cdot \mathbf{a}_j$ , and its inverse is the contravariant metric tensor  $\mathbf{G}^{ij}$ , which can be formally defined as (Warsi 2006)

$$\mathbf{G}^{ij} \equiv \frac{\partial x^i}{\partial x} \frac{\partial x^j}{\partial x} + \frac{\partial x^i}{\partial y} \frac{\partial x^j}{\partial y}; \quad i, j \in \{1, 2\}. \tag{3}$$

Figure 1 schematically shows a nonorthogonal coordinate system  $(x^1, x^2)$  and the covariant and contravariant basis vectors. Note that in Cartesian coordinates, the basis vectors are the unit vectors  $\mathbf{i}$  and  $\mathbf{j}$ . In the case of nonorthogonal coordinate systems, the two sets of basis vectors point in different directions. The covariant basis vector ( $\mathbf{a}_i$ ) corresponding to the  $i$ th dimension is tangent to coordinate lines of the other dimension, while

the contravariant basis vector ( $\mathbf{a}^i$ ) corresponding to the  $i$ th dimension is normal to coordinate lines of that dimension (see Fig. 1).

In the transformed coordinate system, vectors can be expressed as linear combinations of either basis vector set. This gives rise to the covariant velocity components  $(u_1, u_2)$  and the contravariant velocity components  $(u^1, u^2)$ , either set being sufficient to specify the velocity in physical space. By convention, the dimensional indices of covariant vector components are denoted by subscripts, while those of contravariant components are denoted by superscripts. The covariant velocity components are projections of the velocity onto the covariant basis vectors, as given by

$$u_i = \mathbf{u} \cdot \mathbf{a}_i, \tag{4}$$

and the contravariant velocity components are projections of the velocity onto the contravariant basis vectors, as given by

$$u^i = \mathbf{u} \cdot \mathbf{a}^i, \tag{5}$$

where  $\mathbf{u}$  is the velocity. Each set of velocity components can be converted to the other using the metric tensors  $\mathbf{G}^{ij}$  and  $\mathbf{G}_{ij}$  through the following relations:

$$\begin{aligned} \begin{bmatrix} u^1 \\ u^2 \end{bmatrix} &= \begin{bmatrix} G^{11} & G^{12} \\ G^{21} & G^{22} \end{bmatrix} \begin{bmatrix} u_1 \\ u_2 \end{bmatrix} \quad \text{and} \\ \begin{bmatrix} u_1 \\ u_2 \end{bmatrix} &= \begin{bmatrix} G_{11} & G_{12} \\ G_{21} & G_{22} \end{bmatrix} \begin{bmatrix} u^1 \\ u^2 \end{bmatrix}. \end{aligned} \tag{6}$$

The Cartesian  $x$ -component and  $y$ -component velocities,  $u$  and  $v$ , respectively, can be diagnosed from the following equations:

$$\left. \begin{aligned} u &= \left( \frac{\partial x^1}{\partial x} \right) u_1 + \left( \frac{\partial x^2}{\partial x} \right) u_2 \\ v &= \left( \frac{\partial x^1}{\partial y} \right) u_1 + \left( \frac{\partial x^2}{\partial y} \right) u_2 \end{aligned} \right\} \tag{7}$$

Finally, the Jacobian of the coordinate transformation (the metric term), which relates the area elements in each system, is given by

$$\sqrt{G} = |\mathbf{G}_{ij}|^{1/2} = \frac{\partial x}{\partial x^1} \frac{\partial y}{\partial x^2} - \frac{\partial x}{\partial x^2} \frac{\partial y}{\partial x^1}. \tag{8}$$

*b. Shallow-water equations*

The continuity and momentum equations for the shallow-water system (e.g., Sadourny 1972; Nair et al.

2005a; Bao et al. 2014) can be written in generalized curvilinear coordinates as

$$\frac{\partial}{\partial t}(\sqrt{G}h) + \frac{\partial}{\partial x^1}(\sqrt{G}hu^1) + \frac{\partial}{\partial x^2}(\sqrt{G}hu^2) = 0, \quad (9)$$

$$\frac{\partial u_1}{\partial t} + \frac{\partial}{\partial x^1}(K + \Phi) = \sqrt{G}hu^2q, \quad (10)$$

and

$$\frac{\partial u_2}{\partial t} + \frac{\partial}{\partial x^2}(K + \Phi) = -\sqrt{G}hu^1q, \quad (11)$$

where  $h$  is the fluid depth,  $K$  is the kinetic energy, given by

$$K = \frac{1}{2}(u^1u_1 + u^2u_2), \quad (12)$$

and  $\Phi$  is the geopotential of the free surface, defined as

$$\Phi \equiv g(h + h_s), \quad (13)$$

where  $h_s$  is the bottom surface height and  $g$  is the gravitational acceleration. The potential vorticity  $q$  is defined as

$$q \equiv \frac{f + \zeta}{h}, \quad (14)$$

where  $f$  is the Coriolis parameter, and  $\zeta$  is the relative vorticity, given by

$$\zeta = \frac{1}{\sqrt{G}} \left( \frac{\partial u_2}{\partial x^1} - \frac{\partial u_1}{\partial x^2} \right). \quad (15)$$

Equations (10) and (11), which are based on the vector invariant form of the momentum equations, have basically the same form as the Cartesian-coordinate equations in AL81. Note that the vorticity in (15) is naturally defined in terms of the covariant velocity components since they are tangent to coordinate surfaces, while the mass-flux terms of the continuity equation in (9) are written in terms of the contravariant components, which are directed normal to coordinate surfaces. Finally, the product  $\sqrt{G}h$  represents a ‘‘pseudo-density’’ that is related to the amount of mass per unit area in the transformed coordinate system.

We basically follow the same steps as in AL81 to formulate the conservation of integral invariants such as total energy, potential vorticity, and potential enstrophy in the generalized coordinate framework. This will serve as a guide for the discrete derivations in the next section. Multiplying (10) by  $\sqrt{G}hu^1$  and adding (11) multiplied by  $\sqrt{G}hu^2$ , we get

$$\begin{aligned} & \sqrt{G}h \left( u^1 \frac{\partial u_1}{\partial t} + u^2 \frac{\partial u_2}{\partial t} \right) + \sqrt{G}hu^1 \frac{\partial K}{\partial x^1} + \sqrt{G}hu^2 \frac{\partial K}{\partial x^2} \\ & + \sqrt{G}hu^1 \frac{\partial \Phi}{\partial x^1} + \sqrt{G}hu^2 \frac{\partial \Phi}{\partial x^2} = 0. \end{aligned} \quad (16)$$

Using (6) and the fact that the metric tensor is symmetric (i.e.,  $G^{12} = G^{21}$ ), the quantity in parentheses on the lhs of (16) can be rearranged as

$$u^1 \frac{\partial u_1}{\partial t} + u^2 \frac{\partial u_2}{\partial t} = u_1 \frac{\partial u^1}{\partial t} + u_2 \frac{\partial u^2}{\partial t}. \quad (17)$$

Using (12), we see that this is equivalent to the time tendency of kinetic energy:

$$\begin{aligned} u^1 \frac{\partial u_1}{\partial t} + u^2 \frac{\partial u_2}{\partial t} &= \frac{1}{2} \left( u^1 \frac{\partial u_1}{\partial t} + u^2 \frac{\partial u_2}{\partial t} \right) + \frac{1}{2} \left( u_1 \frac{\partial u^1}{\partial t} + u_2 \frac{\partial u^2}{\partial t} \right) \\ &= \frac{\partial}{\partial t} \left[ \frac{1}{2} (u^1u_1 + u^2u_2) \right] \\ &= \frac{\partial K}{\partial t}. \end{aligned} \quad (18)$$

Combining (9), (16), and (18) gives the time tendency of kinetic energy:

$$\begin{aligned} & \frac{\partial}{\partial t}(\sqrt{G}hK) + \frac{\partial}{\partial x^1}(\sqrt{G}hu^1K) + \frac{\partial}{\partial x^2}(\sqrt{G}hu^2K) \\ & + \sqrt{G}hu^1 \frac{\partial \Phi}{\partial x^1} + \sqrt{G}hu^2 \frac{\partial \Phi}{\partial x^2} = 0. \end{aligned} \quad (19)$$

The time tendency of potential energy is obtained by multiplying (9) by  $\Phi$  and rearranging terms to get

$$\begin{aligned} & \frac{\partial}{\partial t} \left[ \sqrt{G}h g \left( \frac{1}{2}h + h_s \right) \right] + \frac{\partial}{\partial x^1}(\sqrt{G}hu^1\Phi) + \frac{\partial}{\partial x^2}(\sqrt{G}hu^2\Phi) \\ & - \sqrt{G}hu^1 \frac{\partial \Phi}{\partial x^1} - \sqrt{G}hu^2 \frac{\partial \Phi}{\partial x^2} = 0. \end{aligned} \quad (20)$$

Adding (19) and (20) results in the cancellation of the energy conversion terms to give the following expression for the time rate of change of total energy:

$$\begin{aligned} & \frac{\partial}{\partial t} \left\{ \sqrt{G}h \left[ K + g \left( \frac{1}{2}h + h_s \right) \right] \right\} + \frac{\partial}{\partial x^1}[\sqrt{G}hu^1(K + \Phi)] \\ & + \frac{\partial}{\partial x^2}[\sqrt{G}hu^2(K + \Phi)] = 0. \end{aligned} \quad (21)$$

Integrating (21) over the domain results in the following statement of the conservation of total energy:

$$\frac{\partial}{\partial t} \left\{ \sqrt{G}h \left[ K + g \left( \frac{1}{2}h + h_s \right) \right] \right\} = 0, \quad (22)$$

where the overbar represents the area integral in  $x^1$  and  $x^2$  over an infinite domain or over a finite domain with no-flow or periodic boundary conditions.

The potential vorticity equation is obtained by combining (10), (11), (14), and (15) to get

$$\frac{\partial}{\partial t}(\sqrt{G}hq) + \frac{\partial}{\partial x^1}(\sqrt{G}hu^1q) + \frac{\partial}{\partial x^2}(\sqrt{G}hu^2q) = 0. \quad (23)$$

This result shows that potential vorticity is globally conserved. Subtracting (9) times  $q$  from (23) and dividing by  $\sqrt{G}h$  gives

$$\frac{\partial q}{\partial t} + u^1 \frac{\partial q}{\partial x^1} + u^2 \frac{\partial q}{\partial x^2} = 0. \quad (24)$$

Multiplying (24) by  $\sqrt{G}hq$  and adding the potential enstrophy [ $(1/2)q^2$ ] times (9) gives the equation for the time tendency of potential enstrophy:

$$\begin{aligned} \frac{\partial}{\partial t} \left( \sqrt{G}h \frac{1}{2} q^2 \right) + \frac{\partial}{\partial x^1} \left( \sqrt{G}hu^1 \frac{1}{2} q^2 \right) \\ + \frac{\partial}{\partial x^2} \left( \sqrt{G}hu^2 \frac{1}{2} q^2 \right) = 0, \end{aligned} \quad (25)$$

which, when integrated over the domain, gives an expression for the conservation of potential enstrophy:

$$\frac{\partial}{\partial t} \left( \overline{\sqrt{G}h \frac{1}{2} q^2} \right) = 0. \quad (26)$$

In AL81, a finite-difference scheme was derived for the momentum equations which satisfies the following requirements for both divergent and nondivergent flow: that it be consistent with an advection scheme for potential vorticity such that for a spatially constant  $q$ , there is no time change of  $q$ , as prescribed by (24); and that it satisfy conservation of total energy and potential enstrophy, as given by (22) and (26), respectively. In the following section, we show that, due to the similarity of the governing equations between the Cartesian and generalized curvilinear coordinate systems, it is straightforward to carry over the AL81 scheme to the generalized coordinate framework, especially for potential enstrophy conservation. However, to satisfy total energy conservation requires a new derivation for nonorthogonal coordinate systems due to the form of the kinetic energy given by (12), which involves products of the covariant and contravariant velocity components. The contravariant velocity components must be diagnosed from (6) in such a way that the relation in (17) is satisfied in the spatially discrete system. The difficulty arises due to the

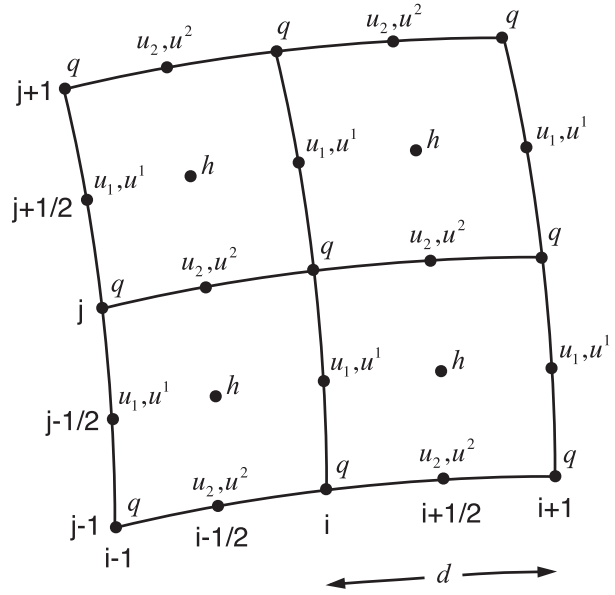


FIG. 2. The Arakawa C grid variable staggering used in the discretization.

grid staggering and the fact that for nonorthogonal coordinates, the off-diagonal terms of the metric tensor (i.e.,  $G^{ij}$  for  $i \neq j$ ) are nonzero.

### 3. Finite-difference equations

In the discrete system we use the Arakawa C grid staggering (Arakawa and Lamb 1977) shown in Fig. 2. Note that the staggering and indexing are the same as in AL81, and that each component of the (predicted) covariant velocity and (diagnosed) contravariant velocity are collocated. For simplicity, the time derivatives will remain in continuous form.

The finite-difference form of the continuity equation in (9) is written as

$$\frac{\partial}{\partial t}(\sqrt{G}h)_{i+1/2,j+1/2} + (\nabla \cdot \mathbf{v}^*)_{i+1/2,j+1/2} = 0, \quad (27)$$

where the mass-flux divergence is given by

$$\begin{aligned} (\nabla \cdot \mathbf{v}^*)_{i+1/2,j+1/2} \equiv \frac{1}{d} [(\sqrt{G}hu^1)_{i+1,j+1/2} - (\sqrt{G}hu^1)_{i,j+1/2} \\ + (\sqrt{G}hu^2)_{i+1/2,j+1} - (\sqrt{G}hu^2)_{i+1/2,j}], \end{aligned} \quad (28)$$

where  $d$  is the grid spacing, assumed to be the same in both dimensions, and the mass fluxes are defined as

$$(\sqrt{G}hu^1)_{i,j+1/2} \equiv [(\sqrt{G}h)^{(u^1)}u^1]_{i,j+1/2}, \quad (29)$$

and

$$(\sqrt{G}hu^2)_{i+1/2,j} \equiv [(\sqrt{G}h)^{(u^2)}u^2]_{i+1/2,j}, \quad (30)$$

where  $(\sqrt{G}h)^{(u^1)}$  and  $(\sqrt{G}h)^{(u^2)}$  are the  $\sqrt{G}$ -weighted fluid depths interpolated to  $u^1$  and  $u^2$  points, respectively. Using the flux-form continuity equation in (27) guarantees mass conservation in the discrete system of equations.

Following AL81, we write the discrete form of the momentum equations in (10) and (11) as

$$\begin{aligned} \frac{\partial}{\partial t}(u_1)_{i,j+1/2} - \alpha_{i,j+1/2}(\sqrt{G}hu^2)_{i+1/2,j+1} - \beta_{i,j+1/2}(\sqrt{G}hu^2)_{i-1/2,j+1} - \gamma_{i,j+1/2}(\sqrt{G}hu^2)_{i-1/2,j} - \delta_{i,j+1/2}(\sqrt{G}hu^2)_{i+1/2,j} \\ + \epsilon_{i+1/2,j+1/2}(\sqrt{G}hu^1)_{i+1,j+1/2} - \epsilon_{i-1/2,j+1/2}(\sqrt{G}hu^1)_{i-1,j+1/2} + \frac{1}{d}[(K + \Phi)_{i+1/2,j+1/2} - (K + \Phi)_{i-1/2,j+1/2}] = 0, \end{aligned} \quad (31)$$

and

$$\begin{aligned} \frac{\partial}{\partial t}(u_2)_{i+1/2,j} + \gamma_{i+1,j+1/2}(\sqrt{G}hu^1)_{i+1,j+1/2} + \delta_{i,j+1/2}(\sqrt{G}hu^1)_{i,j+1/2} + \alpha_{i,j-1/2}(\sqrt{G}hu^1)_{i,j-1/2} + \beta_{i+1,j-1/2}(\sqrt{G}hu^1)_{i+1,j-1/2} \\ + \phi_{i+1/2,j+1/2}(\sqrt{G}hu^2)_{i+1/2,j+1} - \phi_{i+1/2,j-1/2}(\sqrt{G}hu^2)_{i+1/2,j-1} + \frac{1}{d}[(K + \Phi)_{i+1/2,j+1/2} - (K + \Phi)_{i+1/2,j-1/2}] = 0, \end{aligned} \quad (32)$$

where  $\alpha, \beta, \gamma, \delta, \epsilon,$  and  $\phi$  are linear combinations of the potential vorticity  $q$  and  $K$  is defined at  $h$  points.

### a. Conservation of total energy

We now determine the forms of the diagnosed contravariant velocity and kinetic energy required for total energy conservation. Multiplying (31) by  $(\sqrt{G}hu^1)_{i,j+1/2}$  and (32) by  $(\sqrt{G}hu^2)_{i+1/2,j}$ , using (28)–(30), and summing the resulting equations over the domain results in

$$\begin{aligned} \sum_{u^1 \text{ pts}} \frac{\partial}{\partial t} \left[ (\sqrt{G}h)^{(u^1)} \frac{1}{2} u^1 u_1 \right]_{i,j+1/2} + \sum_{u^2 \text{ pts}} \frac{\partial}{\partial t} \left[ (\sqrt{G}h)^{(u^2)} \frac{1}{2} u^2 u_2 \right]_{i+1/2,j} - \sum_{u^1 \text{ pts}} \left[ \frac{1}{2} u^1 u_1 \frac{\partial}{\partial t} (\sqrt{G}h)^{(u^1)} \right]_{i,j+1/2} \\ - \sum_{u^2 \text{ pts}} \left[ \frac{1}{2} u^2 u_2 \frac{\partial}{\partial t} (\sqrt{G}h)^{(u^2)} \right]_{i+1/2,j} - \sum_{h \text{ pts}} [(K + \Phi) \nabla \cdot \mathbf{v}^*]_{i+1/2,j+1/2} + \frac{1}{2} \sum_{u^1 \text{ pts}} (\sqrt{G}h)^{(u^1)}_{i,j+1/2} \left( u^1 \frac{\partial u_1}{\partial t} \right)_{i,j+1/2} \\ + \frac{1}{2} \sum_{u^2 \text{ pts}} (\sqrt{G}h)^{(u^2)}_{i+1/2,j} \left( u^2 \frac{\partial u_2}{\partial t} \right)_{i+1/2,j} - \frac{1}{2} \sum_{u^1 \text{ pts}} (\sqrt{G}h)^{(u^1)}_{i,j+1/2} \left( u_1 \frac{\partial u^1}{\partial t} \right)_{i,j+1/2} - \frac{1}{2} \sum_{u^2 \text{ pts}} (\sqrt{G}h)^{(u^2)}_{i+1/2,j} \left( u_2 \frac{\partial u^2}{\partial t} \right)_{i+1/2,j} = 0, \end{aligned} \quad (33)$$

where we used the identity,

$$\sum_{a \text{ pts}} a_{i,j} (b_{i+1/2,j} - b_{i-1/2,j}) = - \sum_{b \text{ pts}} b_{i+1/2,j} (a_{i+1,j} - a_{i,j}), \quad (34)$$

for two variables  $a$  and  $b$  defined at staggered  $i$  points on the grid, and a similar identity corresponding to the  $j$  index. Note that, as in the continuous equations, the terms involving  $q$  have cancelled out.

In the continuous limit, the last four terms on the lhs of (33) cancel out due to (17). We can achieve cancellation of these terms in the discrete system by properly diagnosing the contravariant velocity components, which we write as the discrete form of (6):

$$(u^1)_{i,j+1/2} = (G^{11})_{i,j+1/2} (u_1)_{i,j+1/2} + (G^{12}u_2)^{(u^1)}_{i,j+1/2}, \quad (35)$$

and

$$(u^2)_{i+1/2,j} = (G^{21}u_1)^{(u^2)}_{i+1/2,j} + (G^{22})_{i+1/2,j} (u_2)_{i+1/2,j}, \quad (36)$$

where  $(G^{12}u_2)^{(u^1)}$  and  $(G^{21}u_1)^{(u^2)}$  are interpolations of four neighboring grid points (see Fig. 2). Using (35) and (36), the requirement for cancellation of the last four terms on the lhs of (33), which is a requirement for energy conservation in the discrete system, becomes

$$\begin{aligned} & \sum_{u^1 \text{ pts}} (\sqrt{Gh})_{ij+1/2}^{(u^1)} (G^{12} u_2)_{ij+1/2}^{(u^1)} \left( \frac{\partial u_1}{\partial t} \right)_{ij+1/2} - \sum_{u^2 \text{ pts}} (\sqrt{Gh})_{i+1/2,j}^{(u^2)} (u_2)_{i+1/2,j} \frac{\partial}{\partial t} (G^{21} u_1)_{i+1/2,j}^{(u^2)} \\ & - \sum_{u^1 \text{ pts}} (\sqrt{Gh})_{ij+1/2}^{(u^1)} (u_1)_{ij+1/2} \frac{\partial}{\partial t} (G^{12} u_2)_{ij+1/2}^{(u^1)} + \sum_{u^2 \text{ pts}} (\sqrt{Gh})_{i+1/2,j}^{(u^2)} (G^{21} u_1)_{i+1/2,j}^{(u^2)} \left( \frac{\partial u_2}{\partial t} \right)_{i+1/2,j} = 0. \end{aligned} \tag{37}$$

We assume that

$$\begin{aligned} (G^{12} u_2)_{ij+1/2}^{(u^1)} = & \frac{1}{(\sqrt{Gh})_{ij+1/2}^{(u^1)}} \left[ \overline{A(G^{12})_{ij+1/2}(G^{12})_{i-1/2,j+1}} \sqrt{(\sqrt{Gh})_{ij+1/2}^{(u^1)} (\sqrt{Gh})_{i-1/2,j+1}^{(u^2)}} (u_2)_{i-1/2,j+1} \right. \\ & + \overline{B(G^{12})_{ij+1/2}(G^{12})_{i+1/2,j+1}} \sqrt{(\sqrt{Gh})_{ij+1/2}^{(u^1)} (\sqrt{Gh})_{i+1/2,j+1}^{(u^2)}} (u_2)_{i+1/2,j+1} \\ & + \overline{C(G^{12})_{ij+1/2}(G^{12})_{i-1/2,j}} \sqrt{(\sqrt{Gh})_{ij+1/2}^{(u^1)} (\sqrt{Gh})_{i-1/2,j}^{(u^2)}} (u_2)_{i-1/2,j} \\ & \left. + \overline{D(G^{12})_{ij+1/2}(G^{12})_{i+1/2,j}} \sqrt{(\sqrt{Gh})_{ij+1/2}^{(u^1)} (\sqrt{Gh})_{i+1/2,j}^{(u^2)}} (u_2)_{i+1/2,j} \right], \end{aligned} \tag{38}$$

and

$$\begin{aligned} (G^{21} u_1)_{i+1/2,j}^{(u^2)} = & \frac{1}{(\sqrt{Gh})_{i+1/2,j}^{(u^2)}} \left[ \overline{E(G^{12})_{i+1/2,j}(G^{12})_{ij+1/2}} \sqrt{(\sqrt{Gh})_{i+1/2,j}^{(u^2)} (\sqrt{Gh})_{ij+1/2}^{(u^1)}} (u_1)_{ij+1/2} \right. \\ & + \overline{F(G^{12})_{i+1/2,j}(G^{12})_{i+1,j+1/2}} \sqrt{(\sqrt{Gh})_{i+1/2,j}^{(u^2)} (\sqrt{Gh})_{i+1,j+1/2}^{(u^1)}} (u_1)_{i+1,j+1/2} \\ & + \overline{G(G^{12})_{i+1/2,j}(G^{12})_{ij-1/2}} \sqrt{(\sqrt{Gh})_{i+1/2,j}^{(u^2)} (\sqrt{Gh})_{ij-1/2}^{(u^1)}} (u_1)_{ij-1/2} \\ & \left. + \overline{H(G^{12})_{i+1/2,j}(G^{12})_{i+1,j-1/2}} \sqrt{(\sqrt{Gh})_{i+1/2,j}^{(u^2)} (\sqrt{Gh})_{i+1,j-1/2}^{(u^1)}} (u_1)_{i+1,j-1/2} \right], \end{aligned} \tag{39}$$

where  $A$  thru  $H$  are constant coefficients and the overbars denote averages of neighboring metric terms. There is freedom to use any form of averaging. In the model, whose results are shown in the next section, we use the arithmetic mean. The inclusion of the fluid depth in the weightings of the covariant velocities is a necessary condition for kinetic energy conservation. Note that in orthogonal coordinates, for which  $G^{12} = G^{21} = 0$ , the rhs of (38) and (39) vanish. Using (38) and (39) in (37), differentiating w.r.t. time, adjusting grid indices, and arranging like terms leads to

---


$$A = H; \quad B = G; \quad C = F; \quad D = E. \tag{40}$$

For consistency, we require

$$A + B + C + D = 1; \quad E + F + G + H = 1. \tag{41}$$

We then choose

$$A = B = C = D = E = F = G = H = 1/4. \tag{42}$$

With the contravariant velocity components given by (35), (36), (38), (39), and (42), we can finally rewrite (33), the time tendency of total kinetic energy, as

---


$$\begin{aligned} & \sum_{u^1 \text{ pts}} \frac{\partial}{\partial t} \left[ (\sqrt{Gh})_{ij+1/2}^{(u^1)} \frac{1}{2} u^1 u_1 \right]_{ij+1/2} + \sum_{u^2 \text{ pts}} \frac{\partial}{\partial t} \left[ (\sqrt{Gh})_{i+1/2,j}^{(u^2)} \frac{1}{2} u^2 u_2 \right]_{i+1/2,j} - \sum_{u^1 \text{ pts}} \left[ \frac{1}{2} u^1 u_1 \frac{\partial}{\partial t} (\sqrt{Gh})_{ij+1/2}^{(u^1)} \right]_{ij+1/2} \\ & - \sum_{u^2 \text{ pts}} \left[ \frac{1}{2} u^2 u_2 \frac{\partial}{\partial t} (\sqrt{Gh})_{i+1/2,j}^{(u^2)} \right]_{i+1/2,j} - \sum_{h \text{ pts}} [(K + \Phi) \nabla \cdot \mathbf{v}^*]_{i+1/2,j+1/2} = 0. \end{aligned} \tag{43}$$

When we choose

$$(\sqrt{Gh})_{ij+1/2}^{(u^1)} = \overline{(\sqrt{Gh})}_{ij+1/2}^i, \quad (44)$$

and

$$(\sqrt{Gh})_{i+1/2,j}^{(u^2)} = \overline{(\sqrt{Gh})}_{i+1/2,j}^j, \quad (45)$$

in the definition of the mass fluxes given by (29) and (30), where the overbars  $\overline{(\ )}^i$  and  $\overline{(\ )}^j$  denote the

arithmetic average of two neighboring points in the  $x^1$  and  $x^2$  directions, respectively, we can use the following identity for any variables  $a$  and  $b$  on a staggered grid,

$$\sum_{\text{apts}} a_{ij}(\bar{b})_{ij} = \sum_{\text{bpts}} b_{i+1/2,j}(\bar{a})_{i+1/2,j}, \quad (46)$$

and the corresponding identity for the  $j$  index, to rewrite (43) as

$$\begin{aligned} & \sum_{\text{hpts}} \frac{\partial}{\partial t} \left[ (\sqrt{Gh}) \frac{1}{2} (\overline{u^1 u^1} + \overline{u^2 u^2}) \right]_{i+1/2,j+1/2} - \sum_{\text{hpts}} (\Phi \nabla \cdot \mathbf{v}^*)_{i+1/2,j+1/2} \\ & - \sum_{\text{hpts}} \left[ \frac{1}{2} (\overline{u^1 u^1} + \overline{u^2 u^2}) \right]_{i+1/2,j+1/2} \frac{\partial}{\partial t} (\sqrt{Gh})_{i+1/2,j+1/2} - \sum_{\text{hpts}} K_{i+1/2,j+1/2} (\nabla \cdot \mathbf{v}^*)_{i+1/2,j+1/2} = 0. \end{aligned} \quad (47)$$

As a result, the discrete form of the kinetic energy is determined by kinetic energy conservation as

$$K_{i+1/2,j+1/2} = \frac{1}{2} (\overline{u^1 u^1} + \overline{u^2 u^2})_{i+1/2,j+1/2}. \quad (48)$$

Using (48) and (27) in (47), the statement of kinetic energy conservation becomes

$$\sum_{\text{hpts}} \frac{\partial}{\partial t} (\sqrt{Gh} K)_{i+1/2,j+1/2} - \sum_{\text{hpts}} (\Phi \nabla \cdot \mathbf{v}^*)_{i+1/2,j+1/2} = 0. \quad (49)$$

The time tendency of total potential energy is obtained by multiplying (27) by  $\Phi_{i+1/2,j+1/2}$  and summing over the domain, which results in

$$\begin{aligned} & \sum_{\text{hpts}} \frac{\partial}{\partial t} \left[ \sqrt{Gh} g \left( \frac{1}{2} h + h_s \right) \right]_{i+1/2,j+1/2} \\ & + \sum_{\text{hpts}} (\Phi \nabla \cdot \mathbf{v}^*)_{i+1/2,j+1/2} = 0. \end{aligned} \quad (50)$$

Adding (49) and (50) shows that total energy is conserved by the discretization:

$$\sum_{\text{hpts}} \frac{\partial}{\partial t} \left\{ \sqrt{Gh} \left[ K + g \left( \frac{1}{2} h + h_s \right) \right] \right\}_{i+1/2,j+1/2} = 0. \quad (51)$$

### b. Conservation of potential enstrophy

The derivation of the discrete form of potential enstrophy conservation follows directly from AL81 when we define the discrete form of  $q$ , defined at  $(i, j)$  points, as

$$q_{ij} \equiv \frac{(f + \zeta)_{ij}}{h_{ij}^{(q)}}, \quad (52)$$

where

$$\zeta_{ij} \equiv \frac{1}{(\sqrt{G})_{i,j} d} [(u_1)_{ij-1/2} - (u_1)_{ij+1/2} + (u_2)_{i+1/2,j} - (u_2)_{i-1/2,j}], \quad (53)$$

$$h_{ij}^{(q)} = \frac{(\sqrt{Gh})_{ij}^{(q)}}{(\sqrt{G})_{ij}}, \quad (54)$$

and

$$\begin{aligned} (\sqrt{Gh})_{ij}^{(q)} &= \frac{1}{4} [(\sqrt{Gh})_{i+1/2,j+1/2} + (\sqrt{Gh})_{i-1/2,j+1/2} \\ &+ (\sqrt{Gh})_{i-1/2,j-1/2} + (\sqrt{Gh})_{i+1/2,j-1/2}]. \end{aligned} \quad (55)$$

Combining (31), (32), and (52)–(54) gives the finite-difference vorticity equation:

$$\begin{aligned}
 \frac{\partial}{\partial t}[(\sqrt{Gh})^{(q)}q]_{ij} = & \frac{1}{d}[-(\sqrt{Ghu}^2)_{i+1/2,j+1}(\alpha_{ij+1/2} + \phi_{i+1/2,j+1/2}) - (\sqrt{Ghu}^2)_{i-1/2,j+1}(\beta_{ij+1/2} - \phi_{i-1/2,j+1/2}) \\
 & + (\sqrt{Ghu}^2)_{i+1/2,j}(\alpha_{ij-1/2} - \delta_{ij+1/2}) + (\sqrt{Ghu}^2)_{i-1/2,j}(\beta_{ij-1/2} - \gamma_{ij+1/2}) \\
 & + (\sqrt{Ghu}^2)_{i+1/2,j-1}(\delta_{ij-1/2} + \phi_{i+1/2,j-1/2}) + (\sqrt{Ghu}^2)_{i-1/2,j-1}(\gamma_{ij-1/2} - \phi_{i-1/2,j-1/2}) \\
 & - (\sqrt{Ghu}^1)_{i+1,j+1/2}(\gamma_{i+1,j+1/2} - \epsilon_{i+1/2,j+1/2}) - (\sqrt{Ghu}^1)_{ij+1/2}(\delta_{ij+1/2} - \gamma_{ij+1/2}) \\
 & + (\sqrt{Ghu}^1)_{i-1,j+1/2}(\delta_{i-1,j+1/2} - \epsilon_{i-1/2,j+1/2}) - (\sqrt{Ghu}^1)_{i+1,j-1/2}(\beta_{i+1,j-1/2} + \epsilon_{i+1/2,j-1/2}) \\
 & - (\sqrt{Ghu}^1)_{ij-1/2}(\alpha_{ij-1/2} - \beta_{ij-1/2}) + (\sqrt{Ghu}^1)_{i-1,j-1/2}(\alpha_{i-1,j-1/2} + \epsilon_{i-1/2,j-1/2})]. \tag{56}
 \end{aligned}$$

Potential vorticity is shown to be globally conserved, as in AL81, by summing (56) over all vorticity points, rearranging indices, and canceling like terms to obtain

$$\sum_{\text{qpts}} \frac{\partial}{\partial t}[(\sqrt{Gh})^{(q)}q]_{ij} = 0. \tag{57}$$

Combining (27), (28), and (55) gives the continuity equation at  $q$  points:

$$\begin{aligned}
 \frac{\partial}{\partial t}(\sqrt{Gh})_{ij}^{(q)} = & -\frac{1}{4d} \{[(\sqrt{Ghu}^2)_{i+1/2,j+1} - (\sqrt{Ghu}^2)_{i+1/2,j} + (\sqrt{Ghu}^1)_{i+1,j+1/2} - (\sqrt{Ghu}^1)_{ij+1/2}] \\
 & + [(\sqrt{Ghu}^2)_{i-1/2,j+1} - (\sqrt{Ghu}^2)_{i-1/2,j} + (\sqrt{Ghu}^1)_{ij+1/2} - (\sqrt{Ghu}^1)_{i-1,j+1/2}] \\
 & + [(\sqrt{Ghu}^2)_{i-1/2,j} - (\sqrt{Ghu}^2)_{i-1/2,j-1} + (\sqrt{Ghu}^1)_{ij-1/2} - (\sqrt{Ghu}^1)_{i-1,j-1/2}] \\
 & + [(\sqrt{Ghu}^2)_{i+1/2,j} - (\sqrt{Ghu}^2)_{i+1/2,j-1} + (\sqrt{Ghu}^1)_{i+1,j-1/2} - (\sqrt{Ghu}^1)_{ij-1/2}]\}. \tag{58}
 \end{aligned}$$

Noting that

$$(\sqrt{Gh})_{ij}^{(q)} \frac{\partial q_{ij}}{\partial t} = \frac{\partial}{\partial t}[(\sqrt{Gh})^{(q)}q]_{ij} - q_{ij} \frac{\partial}{\partial t}(\sqrt{Gh})_{ij}^{(q)}, \tag{59}$$

we can subtract (58) multiplied by  $q_{ij}$  from (56) to get

$$\begin{aligned}
 (\sqrt{Gh})_{ij}^{(q)} \frac{\partial q_{ij}}{\partial t} = & \frac{1}{d} \left[ -(\sqrt{Ghu}^2)_{i+1/2,j+1} \left( \alpha_{ij+1/2} + \phi_{i+1/2,j+1/2} - \frac{q_{ij}}{4} \right) - (\sqrt{Ghu}^2)_{i-1/2,j+1} \left( \beta_{ij+1/2} - \phi_{i-1/2,j+1/2} - \frac{q_{ij}}{4} \right) \right. \\
 & + (\sqrt{Ghu}^2)_{i+1/2,j}(\alpha_{ij-1/2} - \delta_{ij+1/2}) + (\sqrt{Ghu}^2)_{i-1/2,j}(\beta_{ij-1/2} - \gamma_{ij+1/2}) \\
 & + (\sqrt{Ghu}^2)_{i+1/2,j-1} \left( \delta_{ij-1/2} + \phi_{i+1/2,j-1/2} - \frac{q_{ij}}{4} \right) + (\sqrt{Ghu}^2)_{i-1/2,j-1} \left( \gamma_{ij-1/2} - \phi_{i-1/2,j-1/2} - \frac{q_{ij}}{4} \right) \\
 & - (\sqrt{Ghu}^1)_{i+1,j+1/2} \left( \gamma_{i+1,j+1/2} - \epsilon_{i+1/2,j+1/2} - \frac{q_{ij}}{4} \right) - (\sqrt{Ghu}^1)_{ij+1/2}(\delta_{ij+1/2} - \gamma_{ij+1/2}) \\
 & + (\sqrt{Ghu}^1)_{i-1,j+1/2} \left( \delta_{i-1,j+1/2} - \epsilon_{i-1/2,j+1/2} - \frac{q_{ij}}{4} \right) - (\sqrt{Ghu}^1)_{i+1,j-1/2} \left( \beta_{i+1,j-1/2} + \epsilon_{i+1/2,j-1/2} - \frac{q_{ij}}{4} \right) \\
 & \left. - (\sqrt{Ghu}^1)_{ij-1/2}(\alpha_{ij-1/2} - \beta_{ij-1/2}) + (\sqrt{Ghu}^1)_{i-1,j-1/2} \left( \alpha_{i-1,j-1/2} + \epsilon_{i-1/2,j-1/2} - \frac{q_{ij}}{4} \right) \right]. \tag{60}
 \end{aligned}$$

Multiplying (60) by  $q_{i,j}$  and adding  $(1/2)q_{i,j}^2$  times (58) gives the potential enstrophy equation:

$$\begin{aligned} \frac{\partial}{\partial t} \left[ (\sqrt{Gh})^{(q)} \frac{1}{2} q^2 \right]_{i,j} &= \frac{q_{i,j}}{d} \left[ -(\sqrt{Ghu}^2)_{i+1/2,j+1} \left( \alpha_{i,j+1/2} + \phi_{i+1/2,j+1/2} - \frac{q_{i,j}}{8} \right) \right. \\ &\quad - (\sqrt{Ghu}^2)_{i-1/2,j+1} \left( \beta_{i,j+1/2} - \phi_{i-1/2,j+1/2} - \frac{q_{i,j}}{8} \right) + (\sqrt{Ghu}^2)_{i+1/2,j} (\alpha_{i,j-1/2} - \delta_{i,j+1/2}) \\ &\quad + (\sqrt{Ghu}^2)_{i-1/2,j} (\beta_{i,j-1/2} - \gamma_{i,j+1/2}) + (\sqrt{Ghu}^2)_{i+1/2,j-1} \left( \delta_{i,j-1/2} + \phi_{i+1/2,j-1/2} - \frac{q_{i,j}}{8} \right) \\ &\quad + (\sqrt{Ghu}^2)_{i-1/2,j-1} \left( \gamma_{i,j-1/2} - \phi_{i-1/2,j-1/2} - \frac{q_{i,j}}{8} \right) - (\sqrt{Ghu}^1)_{i+1,j+1/2} \left( \gamma_{i+1,j+1/2} - \epsilon_{i+1/2,j+1/2} - \frac{q_{i,j}}{8} \right) \\ &\quad - (\sqrt{Ghu}^1)_{i,j+1/2} (\delta_{i,j+1/2} - \gamma_{i,j+1/2}) + (\sqrt{Ghu}^1)_{i-1,j+1/2} \left( \delta_{i-1,j+1/2} - \epsilon_{i-1/2,j+1/2} - \frac{q_{i,j}}{8} \right) \\ &\quad - (\sqrt{Ghu}^1)_{i+1,j-1/2} \left( \beta_{i+1,j-1/2} + \epsilon_{i+1/2,j-1/2} - \frac{q_{i,j}}{8} \right) - (\sqrt{Ghu}^1)_{i,j-1/2} (\alpha_{i,j-1/2} - \beta_{i,j-1/2}) \\ &\quad \left. + (\sqrt{Ghu}^1)_{i-1,j-1/2} \left( \alpha_{i-1,j-1/2} + \epsilon_{i-1/2,j-1/2} - \frac{q_{i,j}}{8} \right) \right]. \end{aligned} \quad (61)$$

When the linear combinations of potential vorticity are specified as in AL81,

$$\left. \begin{aligned} \epsilon_{i+1/2,j+1/2} &= 1/24(q_{i+1,j+1} + q_{i,j+1} - q_{i,j} - q_{i+1,j}) \\ \phi_{i+1/2,j+1/2} &= 1/24(-q_{i+1,j+1} + q_{i,j+1} + q_{i,j} - q_{i+1,j}) \\ \alpha_{i,j+1/2} &= 1/24(2q_{i+1,j+1} + q_{i,j+1} + 2q_{i,j} + q_{i+1,j}) \\ \beta_{i,j+1/2} &= 1/24(q_{i,j+1} + 2q_{i-1,j+1} + q_{i-1,j} + 2q_{i,j}) \\ \gamma_{i,j+1/2} &= 1/24(2q_{i,j+1} + q_{i-1,j+1} + 2q_{i-1,j} + q_{i,j}) \\ \delta_{i,j+1/2} &= 1/24(q_{i+1,j+1} + 2q_{i,j+1} + q_{i,j} + 2q_{i+1,j}) \end{aligned} \right\}, \quad (62)$$

and they are used in (61) and summed over the domain, the result is the following statement of the conservation of potential enstrophy:

$$\sum_{q\text{pts}} \frac{\partial}{\partial t} \left[ (\sqrt{Gh})^{(q)} \frac{1}{2} q^2 \right]_{i,j} = 0. \quad (63)$$

In summary, (27)–(32), (35), (36), (38), (39), (42), (44), (45), (48), (52)–(55), and (62) describe the energy and potential enstrophy conserving scheme for the shallow-water equations in generalized curvilinear coordinates. In Cartesian coordinates, the scheme reduces exactly to AL81. We should also note that the scheme satisfies the requirement that there be no time change of potential vorticity for a spatially constant  $q$ , which follows from the continuous potential vorticity equation in (24), since the rhs of (60) vanishes for a constant  $q$  applied in (62).

#### 4. Results on a plane surface

The shallow-water equations described in the previous sections are based on the vector invariant form of the momentum equations, which can be used on curved surfaces, such as the sphere. In this section, for simplicity, we test the finite-difference scheme on a plane surface with doubly periodic lateral boundary conditions and prescribe a simple nonorthogonal coordinate transformation that is also doubly periodic. We examine the linear aspects of the discretized system and evaluate the conservation properties in a nonlinear simulation. Results are compared between the nonorthogonal curvilinear coordinate and Cartesian coordinates, in which the scheme is equivalent to AL81.

##### a. Description of the domain and coordinate transformation

The 2D model domain is a flat plane that extends a distance of  $2\pi a$  in each Cartesian ( $x, y$ ) dimension, where  $a = 6.37 \times 10^6$  m is Earth's radius, and the lateral boundaries are doubly periodic. The coordinate transformation used in the experiments is given by

$$\left. \begin{aligned} x^1 &= x + \frac{1}{2} a \sin \frac{y}{a} \\ x^2 &= y + a \sin \frac{x}{a} \end{aligned} \right\}, \quad (64)$$

which is plotted in Fig. 3. This is a simple, nonorthogonal transformation for testing the finite-difference scheme, and is periodic at the lateral boundaries to facilitate evaluation of globally conserved quantities. Note that the transformed coordinate has the units of meters.

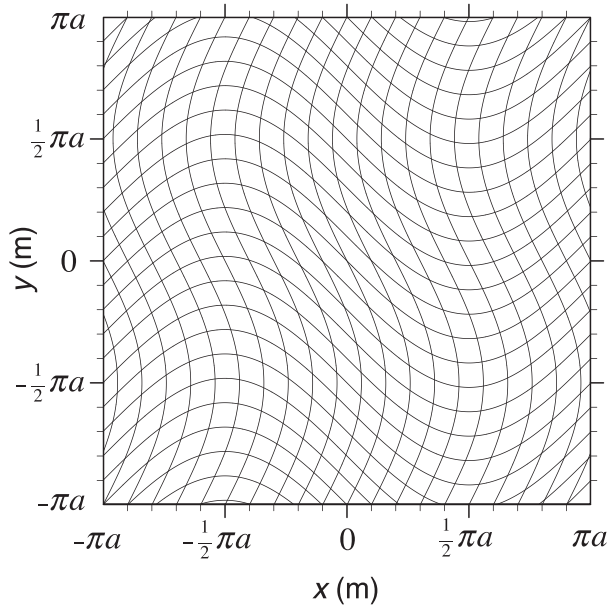


FIG. 3. Isolines of the transformed coordinate plotted in Cartesian coordinates  $(x, y)$ . The contour interval is  $2 \times 10^6$  m.

Coordinate lines are highly nonorthogonal in some areas of the domain, much more so than in typical cubed-sphere grids, so the transformation provides a strong test for the generalized scheme.

Figure 4a shows the Cartesian space, calculated numerically from (64), as a function of the transformed coordinate. The extent of the domain in  $(x^1, x^2)$  coordinates is  $(2\pi a \times 2\pi a)$ , so the four corners of the

Cartesian domain (Fig. 3) and the transformed domain (Fig. 4a) are coincident. Since the transformed coordinate is periodic, the physical boundary conditions of the transformed domain are also periodic, even though the Cartesian and transformed domains are spatially distinct. The Jacobian of the transformation is found by using (64) in (8), which gives

$$\sqrt{G} = \frac{1}{1 - \frac{1}{2} \cos \frac{x}{a} \cos \frac{y}{a}}, \tag{65}$$

and is plotted in Fig. 4b. The Jacobian represents the ratio of the elemental areas between the two coordinate systems, which can be seen as the variation of the apparent size of the quadrilateral elements in Fig. 4a and comparing it to  $\sqrt{G}$  plotted in Fig. 4b. The off-diagonal components of the contravariant metric tensor are calculated from (3) and (64) as

$$G^{12} = \cos \frac{x}{a} + \frac{1}{2} \cos \frac{y}{a}, \tag{66}$$

and is plotted in Fig. 4c. Nonzero values of the metric tensor indicate where the transformed coordinate is nonorthogonal, which can be seen by examining Figs. 4a and 4c.

*b. Linear aspects of the scheme*

One of the desirable properties of a numerical scheme is a robust representation of the Coriolis force. In the continuous system, since the force is normal to fluid motion, it contributes no energy to the flow, and there

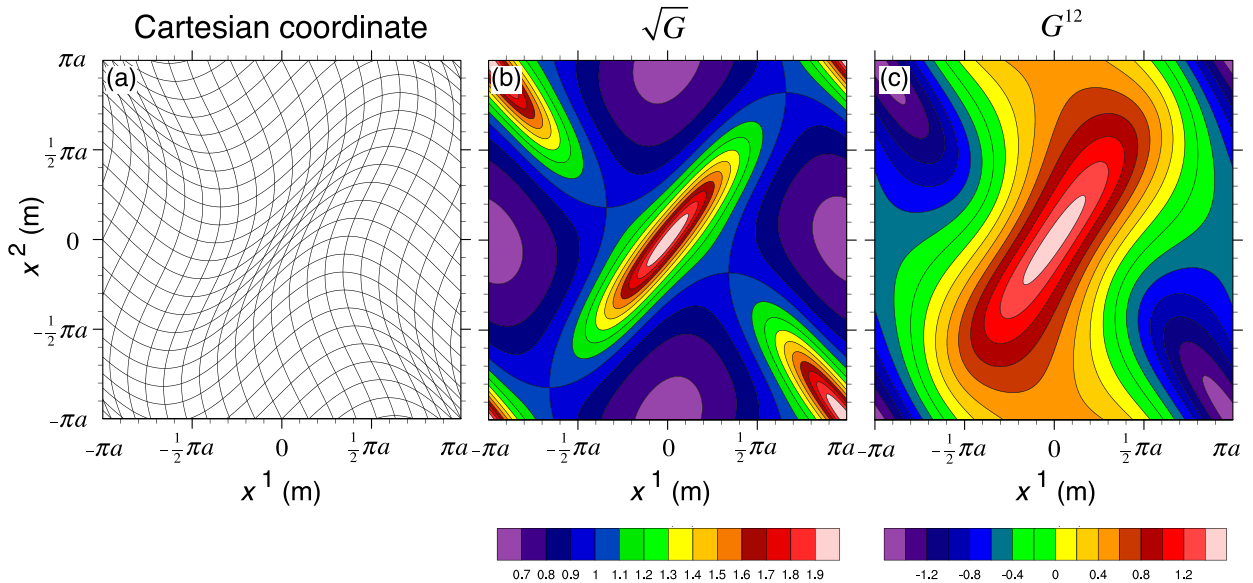


FIG. 4. Coordinate metrics plotted in the transformed coordinate  $(x^1, x^2)$ . (a) Cartesian coordinate isolines with contour interval of  $2 \times 10^6$  m, (b) Jacobian of the transformation  $\sqrt{G}$ , and (c) contravariant metric tensor element  $G^{12}$ .

exist stationary geostrophically balanced modes. However, in discrete systems there is the possibility of nonstationary geostrophic modes (Thuburn 2008; Thuburn et al. 2009; Eldred 2015). The AL81 scheme avoids such artificial nonstationary modes, which is one of its desirable features. Here we determine whether the geostrophically balanced modes are stationary in the scheme extended to generalized, nonorthogonal curvilinear coordinates. Another concern with the generalized scheme that we will investigate is the possible introduction of computational modes due to the four-point averaging of the covariant velocities [Eqs. (38) and (39)] used to diagnose the contravariant velocities.

When we assume a constant Coriolis parameter  $f$ , then the continuous dispersion relation for the  $f$ -plane shallow-water equations linearized about a resting basic state and no bottom topography can be derived analytically (e.g., Randall 1994) as

$$\omega[\omega^2 - gh_0(k^2 + m^2) - f^2] = 0, \quad (67)$$

where  $\omega$  is the frequency,  $h_0$  is the basic-state fluid depth, and  $k$  and  $m$  are the wavenumbers in the  $x$  and  $y$  directions, respectively. The  $\omega = 0$  solutions are the stationary geostrophic modes, while the nonzero-frequency modes correspond to mixed inertio-gravity waves.

The discrete linear system of equations is shown in appendix A. Inspection of the linearized Coriolis terms on the rhs of (A6) and (A7) reveals that the discrete form of the terms are consistent, that is, as the grid spacing vanishes, the metric terms converge to the same value such that (A8) and (A9) converge to the continuous form in (6), causing the Coriolis terms in (A6) and (A7) to converge to the continuous forms  $\sqrt{G}fu^2$  and  $-\sqrt{G}fv^1$ , respectively. For the normal-mode analysis, we assume that the time-dependent part of the solution has the form  $e^{i\omega t}$ , so we can write

$$\left. \begin{aligned} \frac{\partial}{\partial t}(h)_{i+1/2,j+1/2} &= i\omega(h)_{i+1/2,j+1/2} \\ \frac{\partial}{\partial t}(u_1)_{i,j+1/2} &= i\omega(u_1)_{i,j+1/2} \\ \frac{\partial}{\partial t}(u_2)_{i+1/2,j} &= i\omega(u_2)_{i+1/2,j} \end{aligned} \right\}. \quad (68)$$

The system in (A5)–(A9) for  $i = 1, 2, 3, \dots, N$  and  $j = 1, 2, 3, \dots, N$ , where  $N$  is the number of grid points in each dimension, then forms an eigenvalue problem in which the eigenvalues  $\omega$  are the normal mode frequencies. The existence of nonzero imaginary components of  $\omega$  imply exponential growth of unstable modes.

We computed the eigenmodes numerically for the domain described in section 4a with  $16 \times 16$  evenly

spaced grid points, giving a spacing of  $d = (1/8)\pi a$  in each coordinate direction. The Coriolis parameter was set to  $f = 0.0001 \text{ s}^{-1}$ , a value of  $g = 9.81 \text{ m s}^{-2}$  was used for gravity, and the basic-state fluid depth was  $h_0 = 5960 \text{ m}$ . We computed the normal modes for Cartesian coordinates by setting  $\sqrt{G} = G^{11} = G^{22} = 1$  and  $G^{12} = 0$ ; for the nonorthogonal coordinate transformation, we used (64). For both coordinate systems, all the imaginary components of frequency were found to be zero within round-off error, and the geostrophic modes were stationary (i.e.,  $\omega = 0$ ) also to within round-off error. In appendix B, we show analytically that the nondivergent geostrophic modes are indeed stationary. Therefore, the AL81 scheme extended to nonorthogonal, curvilinear coordinates does not introduce unstable computational modes or nonstationary geostrophic modes.

The dispersion relations for the discrete system in each coordinate as well as for the continuous system [cf. (67)] are shown in Fig. 5. In each of the two discrete systems, there are a total of  $3N^2 = 768$  modes, with  $2N^2 = 512$  mixed inertio-gravity wave modes with nonzero frequency, and  $N^2 = 256$  stationary, geostrophically balanced modes. The possible wavenumbers are  $\{k, m\} = \{n_x, n_y\}/a$ , where  $n_x$  and  $n_y$  are the integers  $0, 1, 2, \dots, N/2$ . The discrete wavenumbers were determined by Fourier analysis of the eigenvectors. The continuous modes shown in Fig. 5 are ordered by the wavenumbers corresponding to the Cartesian coordinate eigenmodes. They appear to be discontinuous only because the frequencies of the discrete modes are not directly proportional to wavenumber due to the anisotropy introduced by the discrete 2D grid, particularly at high wavenumbers. The frequency error becomes larger for higher wavenumbers. The frequency for nonorthogonal coordinates generally appears to be more accurate, the reason for which is not clear; a possibility may be due to the enhanced grid resolution in some areas of the nonorthogonal coordinate domain (see Fig. 3). While this may enhance the accuracy of the eigenmode frequencies, this is not to say that the accuracy of the eigenvectors is higher. Meanwhile, with decreasing wavenumber (larger wavelength) the discrete and continuous frequencies all converge to the Coriolis frequency.

### c. Nonlinear flow over an isolated mountain

To test the nonlinear aspects of the model, we simulated the flow over an isolated mountain following test case 5 of Williamson et al. (1992). Although this test was designed for use on the sphere, here we apply it to the flat plane described earlier, but with a varying Coriolis parameter given by

$$f(y) = 2\Omega \sin \frac{y}{a}, \quad (69)$$

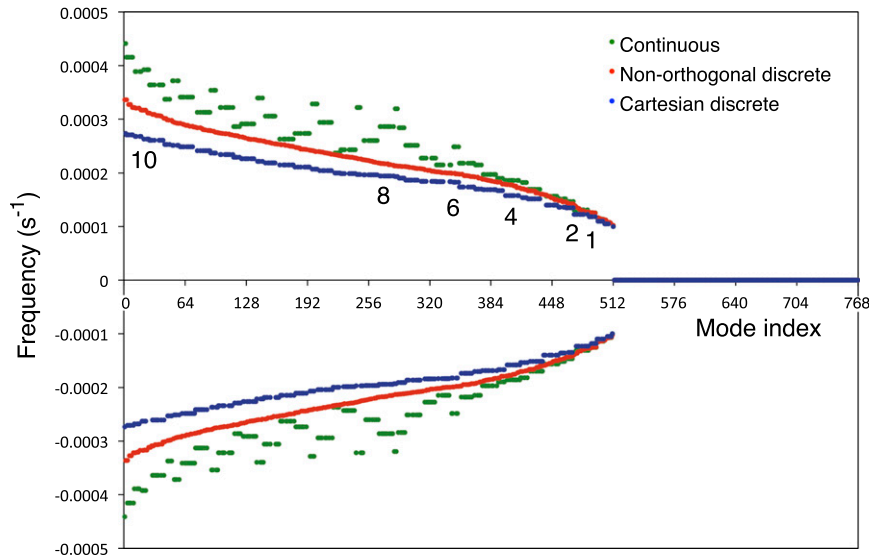


FIG. 5. Normal mode frequencies on the  $f$  plane. The discrete modes (blue and red dots) are ordered by frequency; while the continuous modes (green dots) are arranged to correspond with the eigenmode wavenumbers of the discrete Cartesian eigenmodes (blue dots). The red dots are for the nonorthogonal mode. Modes 1–512 are mixed inertio-gravity waves and modes 513–768 are geostrophically balanced modes. The numbers 10, 8, 6, . . . , 1 denote wavenumber, given by  $(n_x^2 + n_y^2)^{1/2}$ .

where  $\Omega = 7.292 \times 10^{-5} \text{ s}^{-1}$  is the rotation rate of Earth. Note that the Coriolis parameter is periodic in the  $y$  domain, which spans  $\{-\pi a \leq y \leq \pi a\}$ . Physically, this is twice the great-circle distance between Earth’s poles, therefore, the domain is topologically and geometrically equivalent to a rotating cylinder with the same radius as Earth. In the zonal ( $x$ ) direction, the domain has the same extent as Earth’s circumference.

The initial flow is purely zonal with the following profile in  $y$ :

$$u(y) = u_0 \cos \frac{y}{a}, \tag{70}$$

where  $u_0 = 20 \text{ m s}^{-1}$ . The initial free surface geopotential is in geostrophic balance with the flow field and is expressed analytically as

$$\Phi = gh_0 - a\Omega u_0 \sin^2 \frac{y}{a}, \tag{71}$$

where  $h_0 = 5960 \text{ m}$ . The surface height of the mountain is given by

$$h_s = h_{s,0} \left(1 - \frac{r}{R}\right), \tag{72}$$

where  $h_{s,0} = 2000 \text{ m}$ ,  $R = \pi a/9$ , and  $r^2 = \min[R^2, (x - x_c)^2 + (y - y_c)^2]$ . The center of the mountain is located at  $x_c = -\pi a/2$  and  $y_c = \pi a/6$ .

We ran the experiment with both the Cartesian coordinate and the nonorthogonal coordinate with  $400 \times 400$  grid points (with equal coordinate increments) for a grid spacing of  $\approx 100 \text{ km}$  in each coordinate system. In the Cartesian coordinate model the grid points are evenly distributed in physical space, while in the nonorthogonal coordinate, the resolution varies in physical space across the domain (cf. Figs. 3 and 4). The third-order Adams–Bashforth time discretization (Durrant 1991) is used with a time step of 30 s. There is no diffusion included in the models. The relative vorticity ( $\zeta$ ) fields at day 7 of the simulation are shown in Fig. 6. A wave train has developed downstream of the mountain due to the impingement of the flow on the mountain. The field in Fig. 6b is from the nonorthogonal coordinate model and is plotted in the native coordinate. The features of the field in the center of the domain appear stretched due to the coarser resolution and non-orthogonality of the grid in this region (see Fig. 3). When the field is interpolated onto the Cartesian grid (Fig. 6c), the results look similar to the Cartesian coordinate model field shown in Fig. 6a. The results of these simulations on a flat plane look remarkably similar to those of the actual Williamson et al. (1992) test case 5 on the sphere (e.g., Nair 2009).

To compare the model error between the two coordinate systems, we performed a simulation in Cartesian coordinates at a very high resolution ( $\approx 25 \text{ km}$  grid

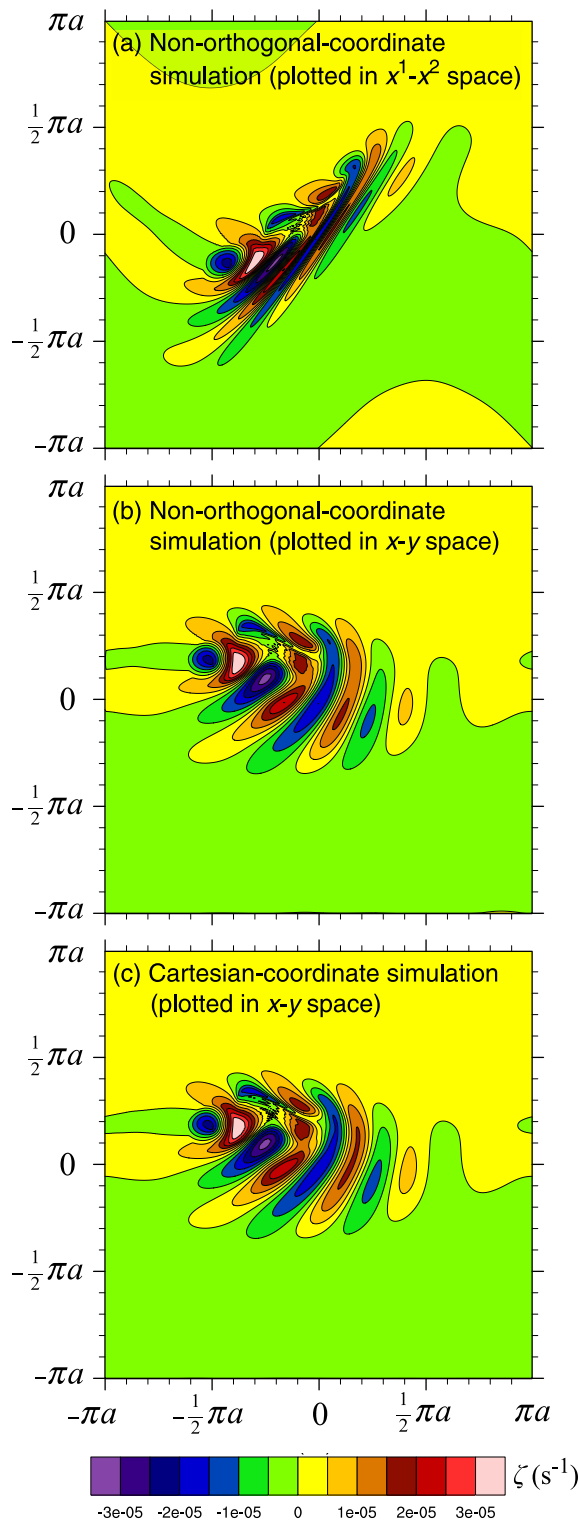


FIG. 6. Relative vorticity  $\zeta$  ( $\text{s}^{-1}$ ) at day 7 for the flow over an isolated mountain: (a) nonorthogonal coordinate simulation, (b) nonorthogonal coordinate simulation interpolated to Cartesian coordinates, and (c) Cartesian coordinate simulation.

spacing) to serve as the “true” solution. The models were run at resolutions 400, 200, and 100 km and the  $L_1$ ,  $L_2$  and  $L_\infty$  error norms, as defined in Williamson et al. (1992), were calculated with respect to the true solution after interpolating the results on to the high-resolution Cartesian grid. Note that the resolution in non-orthogonal coordinates [expressed in km, cf. (64)] corresponds to that in Cartesian coordinates in terms of number of grid points. In physical space, the non-orthogonal grid spacing varies, while in computational space it is constant. All model runs were performed at a small time step (1 s) to minimize the effect of time discretization errors. Figure 7 shows the surface height ( $h_s + h$ ) error convergence for Cartesian coordinates (i.e., AL81’s scheme) versus the generalized scheme in nonorthogonal coordinates. The scheme in Cartesian coordinates converges at a rate between first and second order. The error of the scheme in nonorthogonal coordinates is roughly doubled relative to Cartesian coordinates and the error convergence rate is slightly lower (closer to first order). A possible contributor to the degraded error convergence is the coarser resolution of the nonorthogonal coordinate grid in certain areas, which may not be compensated by areas where the resolution is higher. As noted earlier, the transformed coordinate used in these runs is a strong test of the generalized scheme because of the highly distorted (nonorthogonal) nature of the grid. Cubed-sphere grids, such as those based on equiangular projections (e.g., Nair et al. 2005a), are not as inhomogeneous, and we expect the error characteristics to be more favorable than those shown here.

Finally, we analyzed the total energy and potential enstrophy budgets as realized in the simulations for both coordinate systems. A time series of the global energy budget for the 100-km-resolution simulations is shown in Fig. 8. The changes in geopotential, kinetic, and total (geopotential + kinetic) energy from their initial values are plotted; the conversion of geopotential energy to kinetic energy is apparent. Note that the change in total energy is on the order of  $10^{-6}$  times smaller than the change in kinetic and geopotential energy at a time step of 30 s. When the time step is reduced to 6 s, the change in total energy is much smaller, empirically verifying that total energy is conserved in both Cartesian and nonorthogonal coordinates to within time truncation error. Figure 9 shows a similar plot for the globally averaged potential enstrophy, which is a benchmark for the error in enstrophy conservation. Comparing the change of potential enstrophy with a time step of 30 and 6 s, it appears to be conserved to within time truncation error. The conservation of these integral invariants was expected for Cartesian coordinates (i.e., for the original scheme in AL81). The results with the generalized

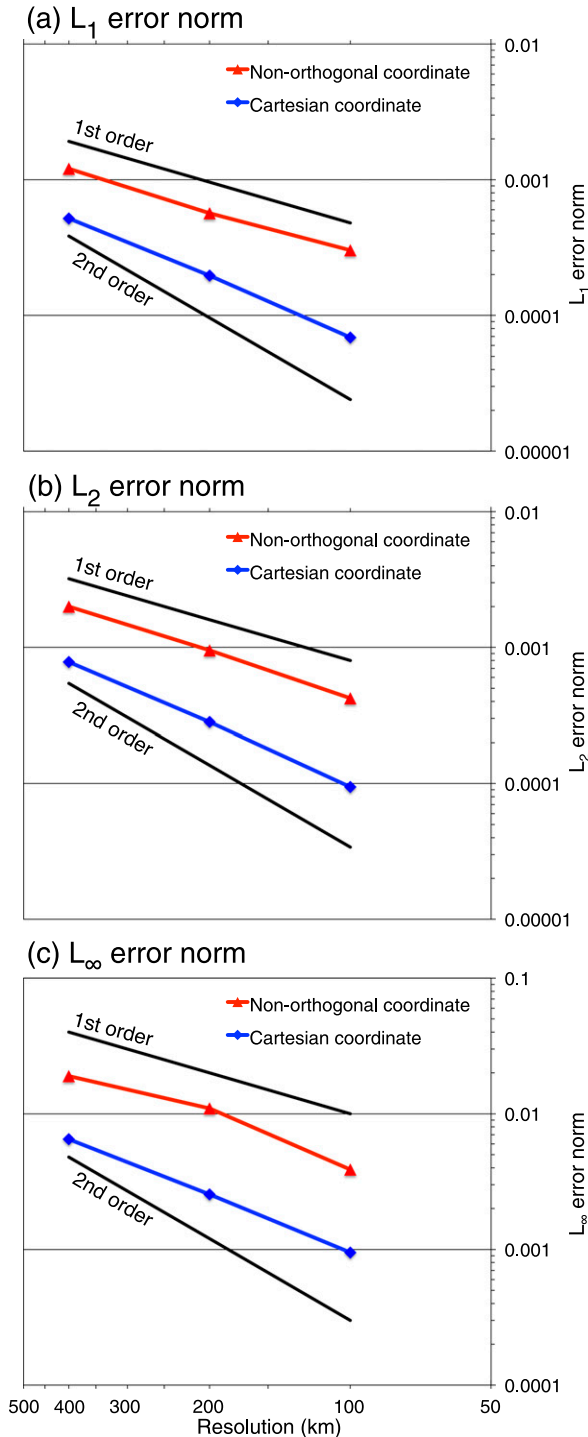


FIG. 7. Convergence of (a)  $L_1$ , (b)  $L_2$ , and (c)  $L_\infty$  error norms for the free surface height ( $h_s + h$ ) at day 7 with increasing grid resolution for flow over an isolated mountain. The Cartesian coordinate results are shown by the blue curves and the nonorthogonal coordinate results are shown by the red curves. First- and second-order convergence are shown for reference as black curves.

curvilinear coordinate verify that the invariants are conserved under the new extended scheme.

*d. Steady-state nonlinear zonal geostrophic flow: Analysis of discretization and local truncation errors*

Removing the mountain in the previous experiment gives a steady-state analytical solution equal to the initial geostrophically balanced flow field, given by (70) and (71). This results in a planar version of test case 2 of Williamson et al. (1992) and is useful for determining discretization errors since any deviation from the initial condition is due to truncation errors of the discrete equations. In this subsection, we analyze the discretization errors of a 7-day simulation, as well as the local truncation errors and convergence properties of the various discrete operators following Weller (2014), Thuburn et al. (2014), and Peixoto (2016).

We ran the experiment for seven simulated days with both the Cartesian coordinate and the nonorthogonal coordinate from the previous experiments at the following horizontal resolutions: 400, 200, 100, 50, and 25 km. Figure 10 shows the resulting  $L_2$  and  $L_\infty$  error norms for the surface height field. Note that the  $L_1$  error norms are very similar to these norms and have been omitted from the figure. The error convergence is second order for both coordinate systems. For the AL81 scheme in Cartesian coordinates, this order of convergence is expected as the discretization consists of centered spatial differencing and averaging, known to be of second-order accuracy. Of note is the fact that the generalized scheme, despite its more complicated form and the inclusion of metric terms, still consists of only centered differences and averages, so second-order accuracy should be expected.

To verify the second-order error convergence of the generalized AL81 scheme, we evaluated the local truncation errors of the nonlinear terms of the discrete equations by comparing the numerical value of each discrete term to its analytical counterpart, given the prescribed field in (70) and (71). The coordinate transformation is given by (64). Equation (71) was evaluated at grid points to give the height field, and the covariant velocities ( $u_1, u_2$ ) were calculated using (70) in (4). The analytical height and covariant velocities at grid points were used to evaluate the discrete terms, starting with the contravariant velocity components ( $u^1, u^2$ ) evaluated using (35) and (36) with (38)–(42). Figure 11a shows that the error convergence for the contravariant velocity diagnosis is second order. Similarly, as shown in Figs. 11b–e, the following terms are also second-order accurate: the mass-flux divergence given by (28); the energy gradient terms [i.e., the last terms on the lhs of

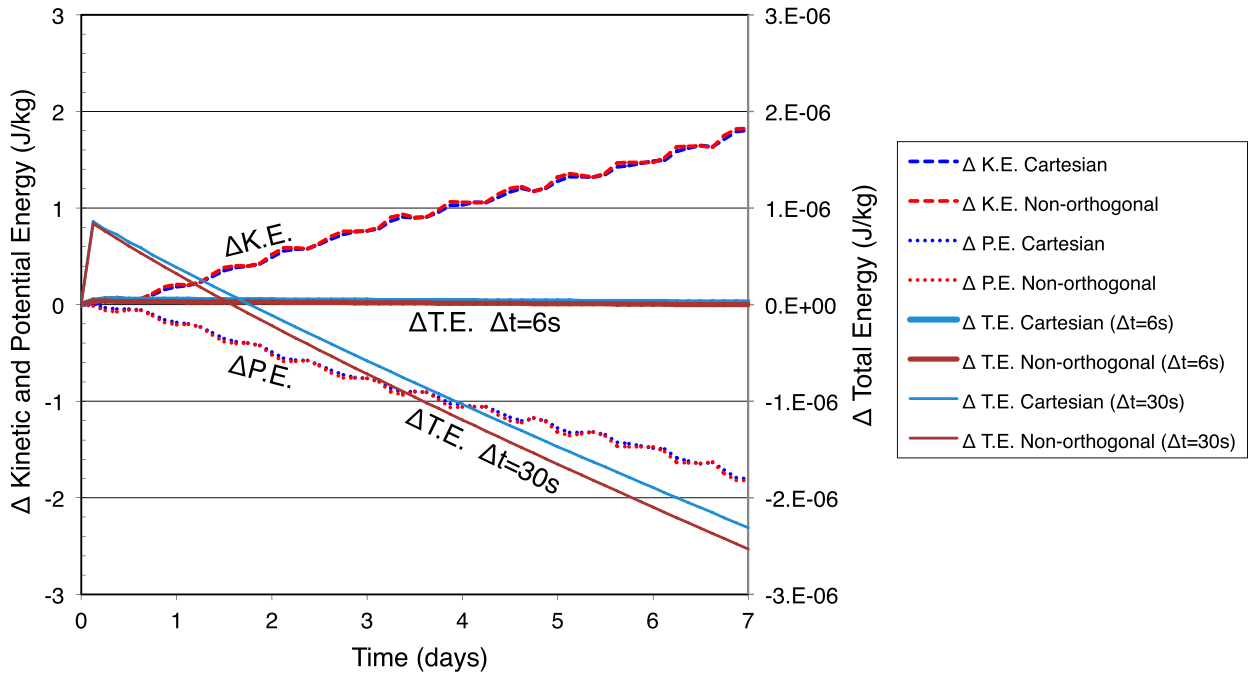


FIG. 8. Time series of the global mean energy budget for flow over an isolated mountain with both coordinate systems showing the changes in kinetic and geopotential energy from their initial values with a time step of 30 s. The change in total (kinetic + geopotential) energy is shown with time steps of 30 and 6 s.

(31) and (32)]; the discrete analog of the “vorticity terms” ( $-\sqrt{Gu^1}\zeta$ ,  $\sqrt{Gu^2}\zeta$ ) given by (31), (32), and (62) with  $\zeta$  substituted for the absolute velocity in the numerator on the rhs of (52); and the Coriolis terms ( $-\sqrt{Gu^1}f$ ,  $\sqrt{Gu^2}f$ ) given by (31), (32), and (62) with  $f$

substituted for the absolute velocity in the numerator on the rhs of (52). This supports our earlier finding in section 4b that the linearized discrete Coriolis term is consistent. Note that the errors shown in Fig. 11 are normalized except for that of the mass-flux divergence,

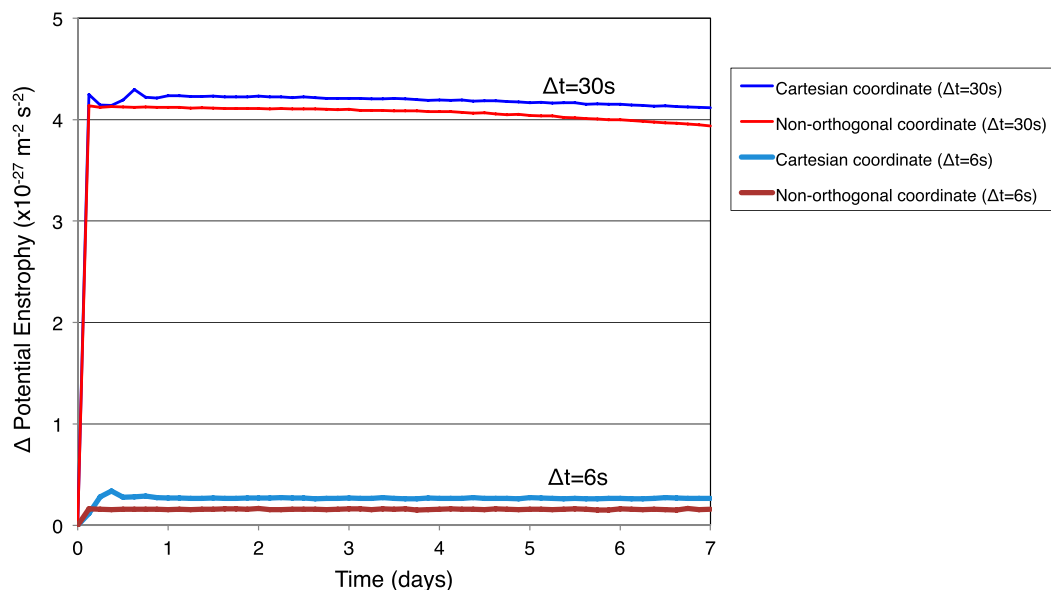


FIG. 9. Time series of the change in global mean potential enstrophy for flow over an isolated mountain with both coordinate systems and with time steps of 30 and 6 s. The Cartesian solution is in darker (lighter) blue and non-orthogonal is in red (purple) for the 30 (6) s steps.

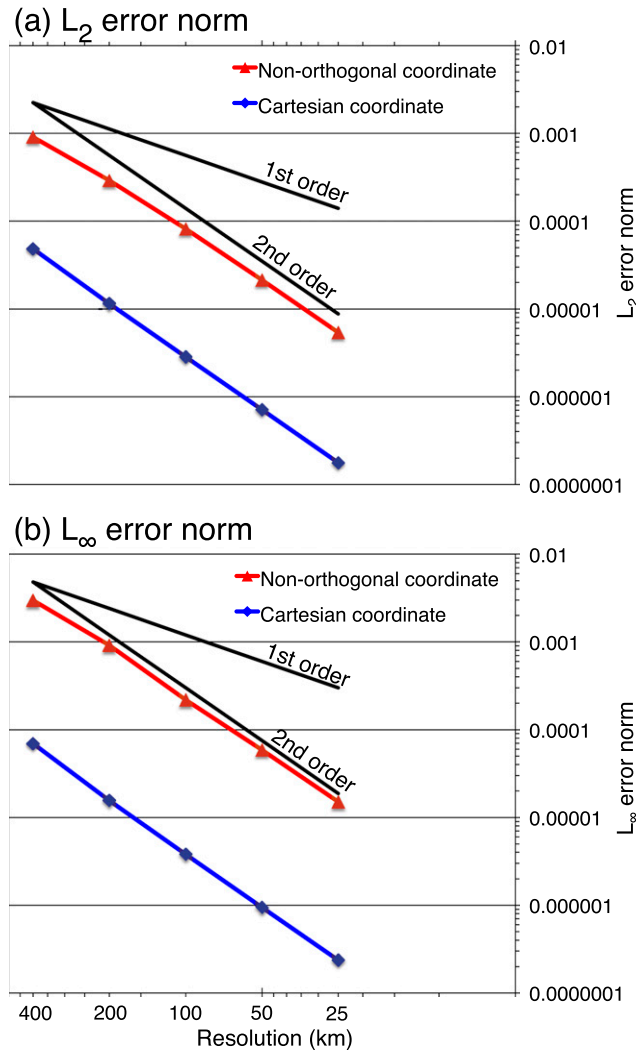


FIG. 10. As in Fig. 7, but for the steady geostrophically balanced (no mountain) test case and the  $L_1$  error norm omitted.

which is the absolute error due to the analytical divergence being zero. Finally, we checked the accuracy of the Laplacian operator on a scalar field prescribed by  $\psi = \sin(x/a) \cos(y/a)$ , following Thuburn et al. (2014). The continuous and discrete forms of the Laplacian operator are shown in appendix C. The accuracy is second order as shown in Fig. 11f, which again is due to the use of centered differences in the discretization.

### 5. Summary and discussion

We have extended the AL81 energy and potential enstrophy conserving finite-difference scheme for the shallow-water equations to generalized curvilinear coordinates. This was done using classical tensor analysis and discretizing the vector-invariant form of the

equations of motion in generalized coordinates. The result is a minor addition to the AL81 scheme, required for energy conservation, which vanishes for rectangular Cartesian coordinates. We simulated the divergent flow over an isolated mountain on a plane surface with doubly-periodic boundary conditions using a nonorthogonal coordinate; the extended scheme was shown to conserve energy and potential enstrophy to within time-truncation error. We compared the resolution-dependent error norm convergence between runs using Cartesian and nonorthogonal coordinates and found that the rates of convergence are comparable (between first and second order), although the error was somewhat larger with the nonorthogonal coordinate, presumably due to coarse resolution and lack of orthogonality of coordinate lines in certain areas of the domain.

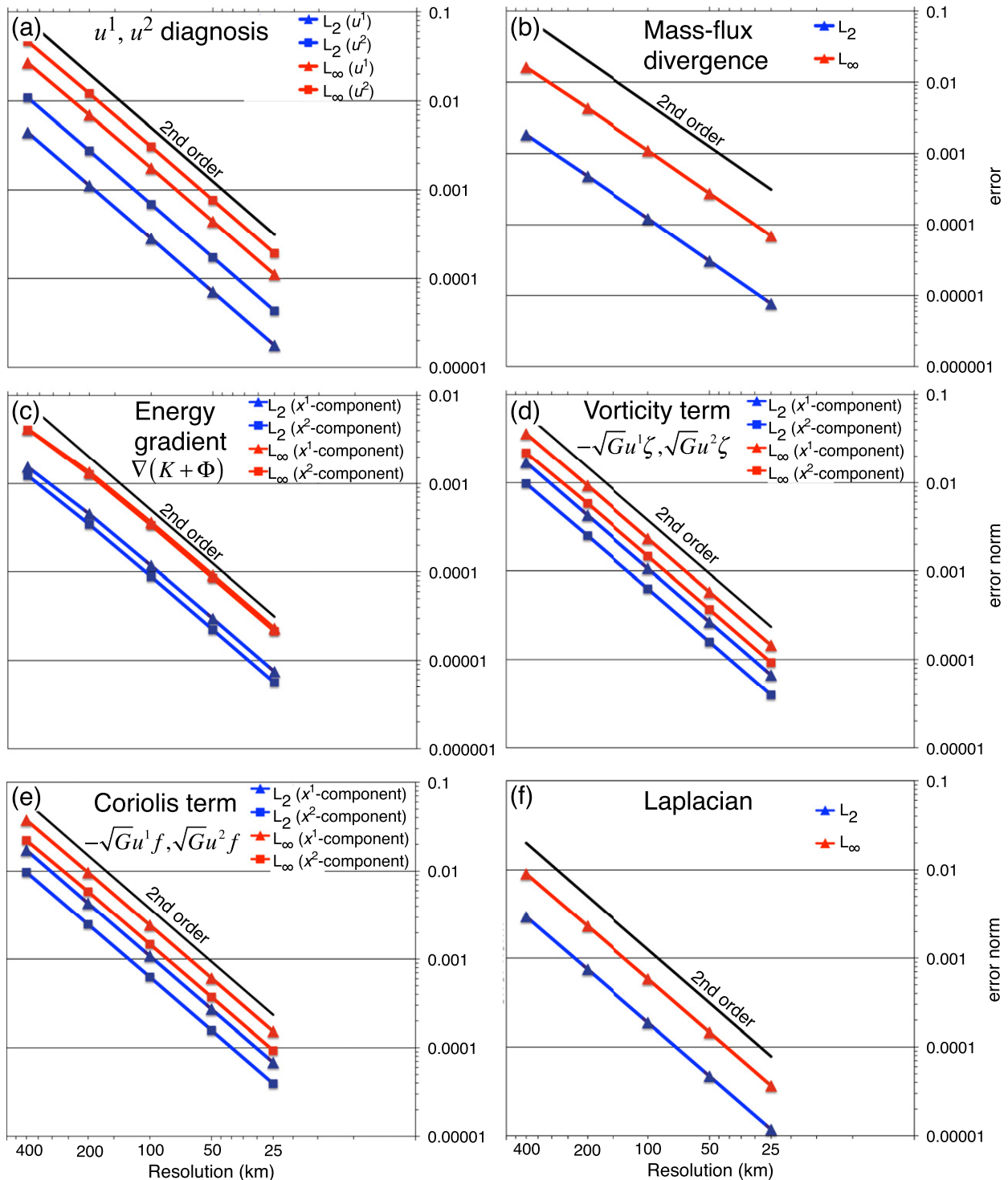


FIG. 11. Resolution-dependent local truncation error of the discrete operators and terms used in the nonorthogonal-coordinate continuity and momentum equations. (a)–(e) Errors are based on the continuous initial velocity and height fields prescribed in the steady geostrophically balanced (no mountain) test case. (f) Errors of the discrete Laplacian operator on a scalar field prescribed as  $\psi = \sin(x/a) \cos(y/a)$ . Note that the errors shown are normalized errors, except for (b), which shows the absolute error.

The AL81 scheme provides a form of the Coriolis term that does not produce unphysical, nonstationary geostrophic modes that are sometimes associated with the Arakawa C grid staggering (Eldred 2015). Like the original scheme, the new scheme extended to generalized curvilinear coordinates provides a consistent form of the Coriolis term. From a normal mode analysis with the nonorthogonal coordinate, it was found that the geostrophic modes remain stationary, that there are no unphysical computational modes introduced by the scheme, and that all of the physical modes are stable. We verified the steadiness of the geostrophic modes by deriving the discrete linear vorticity equation and checking that for nondivergent flow, the vorticity tendency is zero.

The spatial error convergence rates of the nonlinear discrete terms are formally second order owing the use of centered differencing and averaging, as in the original AL81 scheme. We verified this empirically by calculating the local truncation error of each term of the model equations for the geostrophically balanced flow field at varying grid spacing. The error convergence of the height field after a 7-day simulation of the geostrophically balanced flow field was also second order.

As reported by AL81 and Hollingsworth et al. (1983), there is a numerical instability (sometimes referred to as the ‘‘Hollingsworth instability’’) that exists with the AL81 scheme when implemented in 3D models. The instability can be avoided by using an alternative form of the discrete kinetic energy (e.g., AL81). The result is a loss of total energy conservation; however, potential enstrophy is still conserved. We have not yet investigated a stable kinetic energy discretization in generalized curvilinear coordinates, but it will need to be done before implementing the scheme for 3D modeling.

The results of the tests show that the generalized AL81 scheme we have developed could be used advantageously in finite-difference global models using cubed-sphere discretizations. A way to obtain the conservation characteristics, demonstrated in this paper for interior grid points and with periodic boundary conditions, will need to be developed for the interfaces between the six regions representing the cube faces; this is left as work for a forthcoming paper. Also, it may be possible to obtain higher-order accuracy in a generalized-coordinate scheme as was done by Takano and Wurtele (1982) for the AL81 scheme. Finally, we note that while the

generalized grid we used in the paper was based on a mathematically defined coordinate system, as is done on cubed-sphere grids, the scheme may be used with arbitrary quadrilateral grids, which could be used for representing ocean basins. The elements of the metric tensors would then be determined numerically instead of analytically. At that point, further analysis will be needed to determine if the scheme retains second-order accuracy.

*Acknowledgments.* We would like to thank Drs. Hilary Weller, Pedro Peixoto, Christopher Eldred, and one anonymous reviewer for their helpful and constructive comments, which greatly improved the paper. The first author would also like to thank the Institute for Mathematics Applied to Geosciences (IMAGE) at NCAR for their support and collaboration.

## APPENDIX A

### Linearized Discrete System of Equations

The continuous system of equations (9)–(11) linearized about a resting basic state on the  $f$  plane can be written as

$$\frac{\partial h}{\partial t} + \frac{h_0}{\sqrt{G}} \left[ \frac{\partial}{\partial x^1} (\sqrt{G}u^1) + \frac{\partial}{\partial x^2} (\sqrt{G}u^2) \right] = 0, \quad (A1)$$

$$\frac{\partial u_1}{\partial t} = -g \frac{\partial h}{\partial x^1} + \sqrt{G}h_0 u^2 \bar{q}, \quad (A2)$$

and

$$\frac{\partial u_2}{\partial t} = -g \frac{\partial h}{\partial x^2} - \sqrt{G}h_0 u^1 \bar{q}, \quad (A3)$$

where  $h$ ,  $u_1$ , and  $u_2$  refer to perturbation values and  $\bar{q}$  is the basic-state potential vorticity given by

$$\bar{q} = \frac{f}{h_0}. \quad (A4)$$

Applying the finite-difference scheme derived in section 3, the corresponding linearized discrete system simplifies to

$$\begin{aligned} \frac{\partial}{\partial t}(h)_{i+1/2,j+1/2} &= -\frac{h_0}{d} \frac{1}{(\sqrt{G})_{i+1/2,j+1/2}} \left[ (\sqrt{G})_{i+1,j+1/2}^i (u^1)_{i+1,j+1/2} - (\sqrt{G})_{i,j+1/2}^i (u^1)_{i,j+1/2} \right. \\ &\quad \left. + (\sqrt{G})_{i+1/2,j+1}^j (u^2)_{i+1/2,j+1} - (\sqrt{G})_{i+1/2,j}^j (u^2)_{i+1/2,j} \right], \end{aligned} \quad (A5)$$

$$\begin{aligned} \frac{\partial}{\partial t}(u_1)_{i,j+1/2} = & -\frac{g}{d}(h_{i+1/2,j+1/2} - h_{i-1/2,j+1/2}) + \frac{f}{4} [(\overline{\sqrt{G}})_{i+1/2,j+1}^j (u^2)_{i+1/2,j+1} + (\overline{\sqrt{G}})_{i-1/2,j+1}^j (u^2)_{i-1/2,j+1} \\ & + (\overline{\sqrt{G}})_{i-1/2,j}^j (u^2)_{i-1/2,j} + (\overline{\sqrt{G}})_{i+1/2,j}^j (u^2)_{i+1/2,j}], \end{aligned} \quad (\text{A6})$$

and

$$\begin{aligned} \frac{\partial}{\partial t}(u_2)_{i+1/2,j} = & -\frac{g}{d}(h_{i+1/2,j+1/2} - h_{i+1/2,j-1/2}) - \frac{f}{4} [(\overline{\sqrt{G}})_{i+1,j+1/2}^i (u^1)_{i+1,j+1/2} + (\overline{\sqrt{G}})_{i,j+1/2}^i (u^1)_{i,j+1/2} \\ & + (\overline{\sqrt{G}})_{i,j-1/2}^i (u^1)_{i,j-1/2} + (\overline{\sqrt{G}})_{i+1,j-1/2}^i (u^1)_{i+1,j-1/2}], \end{aligned} \quad (\text{A7})$$

where

$$\begin{aligned} (u^1)_{i,j+1/2} = & (G^{11})_{i,j+1/2} (u_1)_{i,j+1/2} + \frac{1}{4} \left[ \frac{(\overline{\sqrt{G}})_{i-1/2,j+1}^j}{(\overline{\sqrt{G}})_{i,j+1/2}^i} \sqrt{\frac{(\overline{\sqrt{G}})_{i-1/2,j+1}^j}{(\overline{\sqrt{G}})_{i,j+1/2}^i}} (u_2)_{i-1/2,j+1} \right. \\ & + \frac{(\overline{\sqrt{G}})_{i+1/2,j+1}^j}{(\overline{\sqrt{G}})_{i,j+1/2}^i} \sqrt{\frac{(\overline{\sqrt{G}})_{i+1/2,j+1}^j}{(\overline{\sqrt{G}})_{i,j+1/2}^i}} (u_2)_{i+1/2,j+1} + \frac{(\overline{\sqrt{G}})_{i-1/2,j}^j}{(\overline{\sqrt{G}})_{i,j+1/2}^i} \sqrt{\frac{(\overline{\sqrt{G}})_{i-1/2,j}^j}{(\overline{\sqrt{G}})_{i,j+1/2}^i}} (u_2)_{i-1/2,j} \\ & \left. + \frac{(\overline{\sqrt{G}})_{i+1/2,j}^j}{(\overline{\sqrt{G}})_{i,j+1/2}^i} \sqrt{\frac{(\overline{\sqrt{G}})_{i+1/2,j}^j}{(\overline{\sqrt{G}})_{i,j+1/2}^i}} (u_2)_{i+1/2,j} \right], \end{aligned} \quad (\text{A8})$$

and

$$\begin{aligned} (u^2)_{i+1/2,j} = & (G^{22})_{i+1/2,j} (u_2)_{i+1/2,j} + \frac{1}{4} \left[ \frac{(\overline{\sqrt{G}})_{i,j+1/2}^i}{(\overline{\sqrt{G}})_{i+1/2,j}^j} \sqrt{\frac{(\overline{\sqrt{G}})_{i,j+1/2}^i}{(\overline{\sqrt{G}})_{i+1/2,j}^j}} (u_1)_{i,j+1/2} \right. \\ & + \frac{(\overline{\sqrt{G}})_{i+1,j+1/2}^i}{(\overline{\sqrt{G}})_{i+1/2,j}^j} \sqrt{\frac{(\overline{\sqrt{G}})_{i+1,j+1/2}^i}{(\overline{\sqrt{G}})_{i+1/2,j}^j}} (u_1)_{i+1,j+1/2} + \frac{(\overline{\sqrt{G}})_{i,j-1/2}^i}{(\overline{\sqrt{G}})_{i+1/2,j}^j} \sqrt{\frac{(\overline{\sqrt{G}})_{i,j-1/2}^i}{(\overline{\sqrt{G}})_{i+1/2,j}^j}} (u_1)_{i,j-1/2} \\ & \left. + \frac{(\overline{\sqrt{G}})_{i+1,j-1/2}^i}{(\overline{\sqrt{G}})_{i+1/2,j}^j} \sqrt{\frac{(\overline{\sqrt{G}})_{i+1,j-1/2}^i}{(\overline{\sqrt{G}})_{i+1/2,j}^j}} (u_1)_{i+1,j-1/2} \right]. \end{aligned} \quad (\text{A9})$$

## APPENDIX B

### Linearized Vorticity and Continuity Equations at $q$ Points

To support the result of our numerical eigendecomposition that the generalized AL81 scheme has stationary

geostrophic modes, we derive the linearized discrete vorticity equation and show that for geostrophic modes, in which the divergence vanishes, the vorticity tendency also vanishes (e.g., Thuburn et al. 2009). The time tendency of the perturbation relative vorticity  $\zeta_{i,j}$  from a resting basic state on the  $f$  plane can be obtained by using (52) and (54) in (56) combined with (62) and (A4) to give

$$\begin{aligned} \frac{\partial}{\partial t}(\sqrt{G}\zeta)_{ij} = &-\frac{f}{4d}[(\sqrt{G}u^2)_{i+1/2,j+1} - (\sqrt{G}u^2)_{i+1/2,j-1} + (\sqrt{G}u^2)_{i-1/2,j+1} - (\sqrt{G}u^2)_{i-1/2,j-1} \\ &+ (\sqrt{G}u^1)_{i+1,j+1/2} - (\sqrt{G}u^1)_{i-1,j+1/2} + (\sqrt{G}u^1)_{i+1,j-1/2} - (\sqrt{G}u^1)_{i-1,j-1/2}], \end{aligned} \tag{B1}$$

where  $u^1$  and  $u^1$  are the perturbation contravariant velocity components. Note that the basic-state fluid depth

$h_0$  has cancelled out. The linearized continuity equation at vorticity points is readily obtained from (58) as

$$\begin{aligned} \frac{\partial}{\partial t}(\sqrt{G}h)_{ij}^{(q)} = &-\frac{h_0}{4d}[(\sqrt{G}u^2)_{i+1/2,j+1} - (\sqrt{G}u^2)_{i+1/2,j-1} + (\sqrt{G}u^2)_{i-1/2,j+1} - (\sqrt{G}u^2)_{i-1/2,j-1} \\ &+ (\sqrt{G}u^1)_{i+1,j+1/2} - (\sqrt{G}u^1)_{i-1,j+1/2} + (\sqrt{G}u^1)_{i+1,j-1/2} - (\sqrt{G}u^1)_{i-1,j-1/2}]. \end{aligned} \tag{B2}$$

When the flow is nondivergent as seen by the fluid depth at mass points, the rhs of (B2) vanishes (i.e., the flow is also nondivergent in terms of continuity at the vorticity points). Therefore, the rhs of (B1) is zero, which confirms that the nondivergent geostrophic modes are steady.

$$\begin{aligned} \nabla^2\psi = &\frac{1}{\sqrt{G}}\left[\frac{\partial}{\partial x^1}\left(\sqrt{G}G^{11}\frac{\partial\psi}{\partial x^1}\right) + \frac{\partial}{\partial x^1}\left(\sqrt{G}G^{12}\frac{\partial\psi}{\partial x^2}\right) \right. \\ &\left. + \frac{\partial}{\partial x^2}\left(\sqrt{G}G^{21}\frac{\partial\psi}{\partial x^1}\right) + \frac{\partial}{\partial x^2}\left(\sqrt{G}G^{22}\frac{\partial\psi}{\partial x^2}\right)\right], \end{aligned} \tag{C1}$$

### APPENDIX C

#### The Laplacian Operator

The Laplacian operator expressed in generalized curvilinear coordinates (e.g., Nair 2009) can be written as follows:

where  $\psi$  is a scalar. The discrete form of (C1) used in the truncation error analysis of section 4d is given by

$$\begin{aligned} (\nabla^2\psi)_{i+1/2,j+1/2} = &\frac{1}{d^2(\sqrt{G})_{i+1/2,j+1/2}}\{[(\sqrt{G}G^{11})_{i+1}(\psi_{i+3/2} - \psi_{i+1/2}) - (\sqrt{G}G^{11})_i(\psi_{i+1/2} - \psi_{i-1/2})]_{j+1/2} \\ &+ [(\sqrt{G}G^{12})_{i+1,j+1/2}(\psi_{i+1,j+1} - \psi_{i+1,j}) - (\sqrt{G}G^{12})_{i,j+1/2}(\psi_{i,j+1} - \psi_{i,j})] \\ &+ [(\sqrt{G}G^{21})_{i+1/2,j+1}(\psi_{i+1,j+1} - \psi_{i,j+1}) - (\sqrt{G}G^{21})_{i+1/2,j}(\psi_{i+1,j} - \psi_{i,j})] \\ &+ [(\sqrt{G}G^{22})_{j+1}(\psi_{j+3/2} - \psi_{j+1/2}) - (\sqrt{G}G^{22})_j(\psi_{j+1/2} - \psi_{j-1/2})]_{i+1/2}\}. \end{aligned} \tag{C2}$$

### REFERENCES

- Adcroft, A., J.-M. Campin, C. Hill, and J. Marshall, 2004: Implementation of an atmosphere–ocean general circulation model on the expanded spherical cube. *Mon. Wea. Rev.*, **132**, 2845–2863, doi:10.1175/MWR2823.1.
- Arakawa, A., and V. R. Lamb, 1977: Computational design of the basic dynamical process of the UCLA general circulation model. *Methods in Computational Physics*, J. Chang, Ed., Vol. 17, Academic Press, 173–265.
- , and —, 1981: A potential enstrophy and energy conserving scheme for the shallow water equations. *Mon. Wea. Rev.*, **109**, 18–36, doi:10.1175/1520-0493(1981)109<0018:APEAEC>2.0.CO;2.
- Bao, L., R. D. Nair, and H. M. Tufo, 2014: A mass and momentum flux-form high-order discontinuous Galerkin shallow water model on the cubed-sphere. *J. Comput. Phys.*, **271**, 224–243, doi:10.1016/j.jcp.2013.11.033.
- Bleck, R., and Coauthors, 2015: A vertically flow-following icosahedral grid model for medium-range and seasonal prediction. Part I: Model description. *Mon. Wea. Rev.*, **143**, 2386–2403, doi:10.1175/MWR-D-14-00300.1.
- Bonaventura, L., and T. Ringler, 2005: Analysis of discrete shallow-water models on geodesic Delaunay grids with C-type staggering. *Mon. Wea. Rev.*, **133**, 2351–2373, doi:10.1175/MWR2986.1.
- Durrant, D. R., 1991: The third-order Adams–Bashforth method: An attractive alternative to leapfrog time differencing. *Mon. Wea. Rev.*, **119**, 702–720, doi:10.1175/1520-0493(1991)119<0702:TTOABM>2.0.CO;2.
- Dutton, J. A., 1986: *The Ceaseless Wind: An Introduction to the Theory of Atmospheric Motion*. Dover Publications, 617 pp.
- Eldred, C., 2015: Linear and nonlinear properties of numerical methods for the rotating shallow water equations. Ph.D. thesis, Colorado State University, 274 pp. [Available online at <http://hdl.handle.net/10217/167080>.]
- Gassmann, A., 2011: Inspection of hexagonal and triangular C-grid discretizations of the shallow water equations. *J. Comput. Phys.*, **230**, 2706–2721, doi:10.1016/j.jcp.2011.01.014.
- Heikes, R., and D. A. Randall, 1995a: Numerical integration of the shallow-water equations on a twisted icosahedral grid. Part I:

- Basic design and results of tests. *Mon. Wea. Rev.*, **123**, 1862–1880, doi:10.1175/1520-0493(1995)123<1862:NIOTSW>2.0.CO;2.
- , and —, 1995b: Numerical integration of the shallow-water equations on a twisted icosahedral grid. Part II: A detailed description of the grid and an analysis of numerical accuracy. *Mon. Wea. Rev.*, **123**, 1881–1887, doi:10.1175/1520-0493(1995)123<1881:NIOTSW>2.0.CO;2.
- Hirani, A. N., 2003: Discrete exterior calculus. Ph.D. thesis, California Institute of Technology, 103 pp. [Available online at [http://thesis.library.caltech.edu/1885/3/thesis\\_hirani.pdf](http://thesis.library.caltech.edu/1885/3/thesis_hirani.pdf).]
- Hollingsworth, A., P. Källberg, V. Renner, and D. M. Burridge, 1983: An internal symmetric computational instability. *Quart. J. Roy. Meteor. Soc.*, **109**, 417–428, doi:10.1002/qj.49710946012.
- Lee, J.-L., and A. E. MacDonald, 2009: A finite-volume icosahedral shallow-water model on a local coordinate. *Mon. Wea. Rev.*, **137**, 1422–1437, doi:10.1175/2008MWR2639.1.
- McGregor, J. L., 1996: Semi-Lagrangian advection on conformal-cubic grids. *Mon. Wea. Rev.*, **124**, 1311–1322, doi:10.1175/1520-0493(1996)124<1311:SLAOCC>2.0.CO;2.
- Nair, R. D., 2009: Diffusion experiments with a global discontinuous Galerkin shallow-water model. *Mon. Wea. Rev.*, **137**, 3339–3350, doi:10.1175/2009MWR2843.1.
- , S. J. Thomas, and R. D. Loft, 2005a: A discontinuous Galerkin global shallow water model. *Mon. Wea. Rev.*, **133**, 876–888, doi:10.1175/MWR2903.1.
- , —, and —, 2005b: A discontinuous Galerkin transport scheme on the cubed sphere. *Mon. Wea. Rev.*, **133**, 814–828, doi:10.1175/MWR2890.1.
- Peixoto, P. S., 2016: Accuracy analysis of mimetic finite volume operators on geodesic grids and a consistent alternative. *J. Comput. Phys.*, **310**, 127–160, doi:10.1016/j.jcp.2015.12.058.
- Rančić, M., R. J. Purser, and F. Mesinger, 1996: A global shallow-water model using an expanded spherical cube: Gnomonic versus conformal coordinates. *Quart. J. Roy. Meteor. Soc.*, **122**, 959–982, doi:10.1002/qj.49712253209.
- Randall, D. A., 1994: Geostrophic adjustment and the finite-difference shallow-water equations. *Mon. Wea. Rev.*, **122**, 1371–1377, doi:10.1175/1520-0493(1994)122<1371:GAATFD>2.0.CO;2.
- Ringler, T. D., and D. A. Randall, 2002: A potential enstrophy and energy conserving numerical scheme for solution of the shallow-water equations on a geodesic grid. *Mon. Wea. Rev.*, **130**, 1397–1410, doi:10.1175/1520-0493(2002)130<1397:APEAEC>2.0.CO;2.
- , J. Thuburn, J. B. Klemp, and W. C. Skamarock, 2010: A unified approach to energy conservation and potential vorticity dynamics for arbitrarily-structured C-grids. *J. Comput. Phys.*, **229**, 3065–3090, doi:10.1016/j.jcp.2009.12.007.
- Ronchi, C., R. Iacono, and P. S. Paolucci, 1996: The “cubed sphere”: A new method for the solution of partial differential equations in spherical geometry. *J. Comput. Phys.*, **124**, 93–114, doi:10.1006/jcph.1996.0047.
- Sadourny, R., 1972: Conservative finite-difference approximations of the primitive equations on quasi-uniform spherical grids. *Mon. Wea. Rev.*, **100**, 136–144, doi:10.1175/1520-0493(1972)100<0136:CFAOTP>2.3.CO;2.
- , A. Arakawa, and Y. Mintz, 1968: Integration of the non-divergent barotropic vorticity equation with an icosahedral-hexagonal grid for the sphere. *Mon. Wea. Rev.*, **96**, 351–356, doi:10.1175/1520-0493(1968)096<0351:IOTNBV>2.0.CO;2.
- Salmon, R., 2004: Poisson-bracket approach to the construction of energy- and potential-enstrophy-conserving algorithms for the shallow-water equations. *J. Atmos. Sci.*, **61**, 2016–2036, doi:10.1175/1520-0469(2004)061<2016:PATTCO>2.0.CO;2.
- , 2007: A general method for conserving energy and potential enstrophy in shallow-water models. *J. Atmos. Sci.*, **64**, 515–531, doi:10.1175/JAS3837.1.
- Satoh, M., T. Matsuno, H. Tomita, H. Miura, T. Nasuno, and S. Iga, 2008: Nonhydrostatic icosahedral atmospheric model (NICAM) for global cloud resolving simulations. *J. Comput. Phys.*, **227**, 3486–3514, doi:10.1016/j.jcp.2007.02.006.
- Stuhne, G. R., and W. R. Peltier, 2006: A robust unstructured grid discretization for 3-dimensional hydrostatic flows in spherical geometry: A new numerical structure for ocean general circulation modeling. *J. Comput. Phys.*, **213**, 704–729, doi:10.1016/j.jcp.2005.08.031.
- Takano, K., and M. G. Wurtele, 1982: A fourth-order energy and potential enstrophy conserving difference scheme. Tech. Rep. AFGL-TR-82-0205, Air Force Geophysics Laboratory, 85 pp.
- Thuburn, J., 2008: Numerical wave propagation on the hexagonal C-grid. *J. Comput. Phys.*, **227**, 5836–5858, doi:10.1016/j.jcp.2008.02.010.
- , and C. J. Cotter, 2012: A framework for mimetic discretization of the rotating shallow-water equations on arbitrary polygonal grids. *SIAM J. Sci. Comput.*, **34**, B203–B225, doi:10.1137/110850293.
- , T. D. Ringler, W. C. Skamarock, and J. B. Klemp, 2009: Numerical representation of geostrophic modes on arbitrarily structured C-grids. *J. Comput. Phys.*, **228**, 8321–8335, doi:10.1016/j.jcp.2009.08.006.
- , C. J. Cotter, and T. Dubos, 2014: A mimetic, semi-implicit, forward-in-time, finite volume shallow water model: Comparison of hexagonal-icosahedral and cubed-sphere grids. *Geosci. Model Dev.*, **7**, 909–929, doi:10.5194/gmd-7-909-2014.
- Tort, M., T. Dubos, and T. Melvin, 2015: Energy-conserving finite-difference schemes for quasi-hydrostatic equations. *Quart. J. Roy. Meteor. Soc.*, **141**, 3056–3075, doi:10.1002/qj.2590.
- Warsi, Z. U. A., 2006: *Fluid Dynamics: Theoretical and Computational Approaches*. 3rd ed. CRC Press, 872 pp.
- Weller, H., 2014: Non-orthogonal version of the arbitrary polygonal C-grid and a new diamond grid. *Geosci. Model Dev.*, **7**, 779–797, doi:10.5194/gmd-7-779-2014.
- Wesseling, P., 2009: *Principles of Computational Fluid Dynamics*. Springer-Verlag, 644 pp.
- Williamson, D. L., 1968: Integration of the barotropic vorticity equation on a spherical geodesic grid. *Tellus*, **20A**, 642–653, doi:10.1111/j.2153-3490.1968.tb00406.x.
- , J. B. Drake, J. J. Hack, R. Jakob, and P. N. Swartztrauber, 1992: A standard test set for numerical approximations to the shallow water equations in spherical geometry. *J. Comput. Phys.*, **102**, 211–224, doi:10.1016/S0021-9991(05)80016-6.